ACSNANO

www.acsnano.org

REVIEW

Airborne Transmission of COVID-19: Aerosol Dispersion, Lung Deposition, and Virus-Receptor Interactions

Yi Y. Zuo,* William E. Uspal,* and Tao Wei*

Cite This: *ACS Nano* 2020, 14, 16502–16524

Read Online

ACCESS | Metrics & More | Article Recommendations

ABSTRACT: Coronavirus disease 2019 (COVID-19), due to infection by the severe acute respiratory syndrome coronavirus 2 (SARS-CoV-2), is now causing a global pandemic. Aerosol transmission of COVID-19, although plausible, has not been confirmed by the World Health Organization (WHO) as a general transmission route. Considering the rapid spread of SARS-CoV-2, especially nosocomial outbreaks and other superspreading events, there is an urgent need to study the possibility of airborne transmission and its impact on the lung, the primary body organ attacked by the virus. Here, we review the complete pathway of airborne transmission of SARS-CoV-2 from aerosol dispersion in air to subsequent biological uptake after inhalation. In particular, we first review the aerodynamic and colloidal mechanisms by which aerosols disperse and transmit in air and deposit onto surfaces. We then review the fundamental mechanisms that govern regional deposition of micro- and nanoparticles in the lung. Focus is given to biophysical interactions between particles and the pulmonary surfactant film, the initial alveolar-capillary barrier and first-line host defense system against inhaled particles and pathogens. Finally, we summarize the current understanding about the structural dynamics of the SARS-CoV-2 spike protein and its interactions with receptors at the atomistic and molecular scales, primarily as revealed by molecular dynamics simulations. This review provides urgent and multidisciplinary knowledge toward understanding the airborne transmission of SARS-CoV-2 and its health impact on the respiratory system.

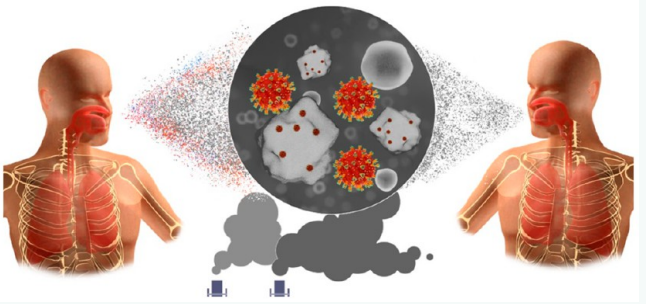

KEYWORDS: *COVID-19, SARS-CoV-2, spike protein, aerosol, particle, lung, pulmonary surfactant, molecular dynamics*

INTRODUCTION

Coronavirus disease 2019 (COVID-19), due to infection of the severe acute respiratory syndrome coronavirus 2 (SARS-CoV-2), is currently causing a global pandemic, with more than 53 million confirmed cases and 1 million deaths, as of November 15, 2020, in more than 200 countries, areas, and territories in the world.[1] Given the current world population of 7.8 billion, approximately 1 out of every 150 humans on earth has or had been infected with COVID-19. The incidence of COVID-19 shows strong ethnic disparities. Emerging epidemiological data suggest that black communities are affected disproportionately hard by COVID-19.[2,3] Although they account for only 13% of the United States population, African Americans constitute 24% of COVID-19 deaths, nearly twice of what would be expected based on their share of the national population.[4] In some regions of the United States, such as Chicago, the death rate of African Americans has been reported to be six times higher than that of the white population.[5] Similarly, it was found that indigenous peoples of the Pacific, including Native Hawaiians and Pacific Islanders, have a significantly higher COVID-19 infection rate than other ethnic groups.[6] These health disparities among racial and ethnic groups are often related to different living conditions, work circumstances, and underlying health conditions including diabetes, heart disease, and lung disease, all of which are closely linked to more severe cases of COVID-19.[7,8]

All available evidence suggests that SARS-CoV-2 is highly contagious and quickly spreads in our communities.[9] To date, the confirmed modes of SARS-CoV-2 transmission include

Received: October 11, 2020
Accepted: November 19, 2020
Published: November 25, 2020

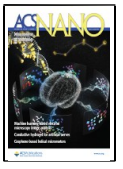

https://dx.doi.org/10.1021/acsnano.0c08484
ACS Nano 2020, 14, 16502–16524

respiratory droplets, direct (person-to-person) and indirect (fomite) contacts, as well as scarce reports of fecal−oral transmission.[10] However, the latest research suggests that fomite transmission is unlikely to be a major route of transmission as attempts to culture SARS-CoV-2 from surfaces were largely unsuccessful.[11,12] On the other hand, airborne transmission of SARS-CoV-2, although plausible, has not been confirmed by the World Health Organization (WHO) as a general transmission route.[10] However, on October 5, 2020, the United States Centers for Disease Control and Prevention (CDC) updated their guideline and acknowledged that airborne transmission of SARS-CoV-2 could occur under special circumstances that include enclosed spaces, inadequate ventilation, and prolonged exposure to events involving heavy breathing, such as singing and exercising.[13] Given the rapid spread of the coronavirus, especially nosocomial outbreaks and other superspreading events, there is an urgent need to carefully access the possibility of airborne transmission, especially the colloidal and aerodynamic mechanisms of aerosol dispersion and deposition, and the molecular interactions between SARS-CoV-2 and receptors.[14−22]

An open letter by 239 researchers from 32 countries, published on July 6, 2020, challenged the WHO's view on aerosol transmission.[23] Virus transmission *via* aerosols can be fundamentally different from transmission *via* respiratory droplets in terms of their colloidal and aerodynamic mechanisms.[24] Respiratory droplets are emitted when an infected individual coughs or sneezes. Due to their large size (usually >5−10 μm), these droplets in general have a very short lifetime in air and a limited transmission distance of <2 m, although some studies suggest that these droplets could travel as far as 8 m.[25] Aerosols, often called droplet nuclei, are airborne particles or droplets much smaller than 5 μm.[24] It should be noted that the aerodynamic size of 5 μm is not a strictly defined threshold, but a historical value that provides a loose definition of aerosols. In contrast to respiratory droplets, it appears that coughs or sneezes are unnecessary for producing infectious aerosols, and simple exhalation is sufficient.[26,27] In general, most aerosols in exhaled breath are found to be are smaller than 4 μm, with a median between 0.7 and 1 μm.[24,28] Also different from respiratory droplets, aerosols are too small to rapidly settle out of the atmosphere under the influence of gravity.[22] Respiratory droplets in the size range between 60 and 100 μm, although could be carried more than 6 m by sneezing, generally fall to the ground within two meters.[24,29] Depending on the environmental conditions, virus particles (*i.e.*, virions) may bind to aerosols and thus travel over a significantly longer distance (>2 m) and remain floating in air for a much longer time period (up to hours) than respiratory droplets. It is now known that air pollution is an associated risk factor of COVID-19.[30,31] An increase of 1 $\mu g/m^3$ in PM2.5 is associated with an 8% increase in the COVID-19 death rate.[32] In addition, it was found that outside the optimal relative humidity (RH) range of 40−60%, the viability of influenza virus in droplets increased both at higher (>60%) and lower (<40%) RH.[33] A similar humidity dependence has been found for the transmission of SARS-CoV-2.[34] E-cigarette aerosols have also been identified as suspicious anthropogenic aerosols potentially capable of spreading SARS-CoV-2.[35,36]

Aerosol transmission was reported to be responsible for a superspreading event of SARS-CoV in a housing block in Hong Kong in 2003.[37,38] The 50-story building had 342 confirmed cases of SARS and 42 deaths. The report identified defects in the wastewater plumbing system as a transmission mode within the building, which facilitated the transport of virus-laden aerosols through empty U-bends in bathrooms. In a superspreading event at a church in Skagit County, WA, 45 out of 60 singers of a choir were diagnosed with COVID-19 with two deaths, after only a 2.5 h rehearsal in which nobody present was coughing or sneezing or appeared ill.[39] Another superspreading event reported in China involved 10 individuals from three families in the same restaurant.[40] This study found that the virus was able to travel far enough to infect individual members of the three families. It appears that virus transmission in this outbreak cannot be explained by droplet transmission alone and consequently might involve aerosol transmission.[40] In fact, although available evidence remains scarce, SARS-CoV-2 has been detected in hospital air.[41,42] A recent study suggested that in every hour COVID-19 patients can exhale millions of SARS-CoV-2 RNA copies into air.[27] Given a study demonstrating that SARS-CoV-2 remained viable in aerosols for at least 3 h with only limited reduction in infectious titer,[43] there is an urgent need to understand the likelihood of SARS-CoV-2 transmission *via* aerosols.

In this paper, we review the complete pathway of airborne transmission of SARS-CoV-2 from aerosol dispersion in air to subsequent biological uptake after inhalation. The review is organized in three main sections. First, we review the aerodynamic and colloidal mechanisms by which aerosols disperse and transmit in air and deposit onto surfaces. Second, we focus on lung deposition of the aerosols and their interaction with the first-line host defense pulmonary surfactant (PS) film at the alveolar−capillary barrier. Third, we summarize the current understanding of molecular interactions between SARS-CoV-2 and receptors. This review provides urgent and multidisciplinary knowledge in understanding the airborne transmission of SARS-CoV-2.

AEROSOL DISPERSION AND DEPOSITION

Basic Considerations. The dispersion of infectious aerosols in air and their subsequent deposition onto surfaces are physical processes that can be modeled by treating air as a continuous medium that exchanges mass, energy, and momentum with the aerosol particles and associated virions. As physical processes, they can potentially be controlled through an engineering approach, for example, by designing interior spaces with controlled ventilation and humidity or by engineering surface coatings that disrupt virus transmission. In this section, we review the literature on the transport of infectious aerosols in the atmosphere and their deposition onto surfaces. In particular, our review is intended to facilitate development of realistic models that capture all relevant physical effects and are parametrized by experimental measurements.

First, we develop some basic considerations concerning SARS-CoV-2 virions and aerosols. Aerosols are commonly defined as solid particles or liquid droplets with diameters between a few nanometers and micrometers. This range includes the smallest e-cigarette aerosols, with characteristic size D = 150 nm, to the largest PM2.5 particles, with D = 5 μm. Given the typical diameter of a SARS-CoV-2 virion at approximately D_v = 70 nm,[44] the size ratio D_v/D can vary from $D_v/D \approx 0.5$ to $D_v/D \approx 0.01$.

The typical number of virions per aerosol is also an important quantity. We are not aware of any study that has sought to directly measure this quantity for aerosols laden with SARS-CoV-2, which must depend on the biophysical process

https://dx.doi.org/10.1021/acsnano.0c08484
ACS Nano 2020, 14, 16502−16524

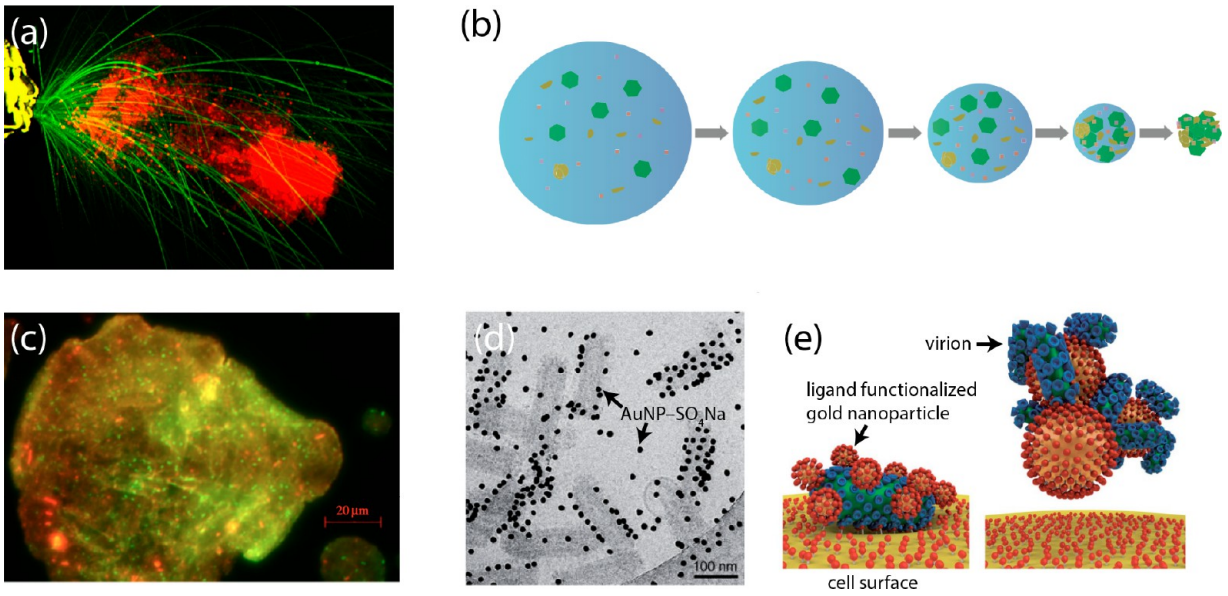

Figure 1. (a) High-speed image of a sneeze. Large drops (green) move ballistically and settle under the influence of gravity. Smaller drops are carried by a moist and buoyant "puff" (red), which can travel for several meters from the emitter. Droplets of a sufficiently small size can evaporate to form dry nuclei (*i.e.*, aerosols) before settling to the ground. Adapted with permission from ref 51. Copyright 2020 Elsevier. (b) Schematic illustration of the temporal evolution of a respiratory droplet as it disperses in the atmosphere. The droplet evaporates over time, eventually reducing to a dry nucleus of biopolymers and virion particles. The various colored shapes schematically represent encapsulated biomaterials, such as proteins, salts, and virions. Adapted with permission from ref 63. Copyright 2008 American Society for Microbiology. (c) Composite fluorescent image of a droplet of model respiratory solution containing phi-6 virions; mucin protein, labeled with red fluorescent dye; DPPC lung surfactant lipid, labeled with green fluorescent dye; and salt (NaCl) on a solid substrate. The lipid (bright green dots) is assumed to partition to the virion particles. Adapted with permission under a Creative Commons Attribution 4.0 License from ref 53. Copyright 2019 Royal Society Publishing. (d) Cyro-TEM image of vesicular stomatitis virion particles with adsorbed nanoparticles. Adapted with permission from ref 67. Copyright 2014 Royal Society of Chemistry. (e) Schematic illustration of a virion and functionalized nanoparticles in the vicinity of a cell membrane. Large nanoparticles (right panel) inhibit cell infection more effectively than small nanoparticles (left). Adapted with permission from ref 67. Copyright 2014 Royal Society of Chemistry.

generating infectious aerosols. Still, some idea of this number can be obtained from other quantitative data on SARS-CoV-2. According to Bar-On *et al.*,[45] COVID-19 patient sputum contains 10^6–10^{11} viral RNAs per milliliter, although this number "can overestimate infectious virions". If sputum matter is aerosolized as 5 μm particles, then the average number of virions per aerosol, using 10^{11} virions/mL, is no greater than 50. The actual number is probably much less than this upper bound. Furthermore, previous studies have sought to characterize the number of virions per aerosol for other viruses. For instance, in a study of artificially generated, infectious aerosols carrying the MS2 bacteriophage, the authors estimated $\sim 10^{-4}$ virions per aerosol particle.[46] Since this is a sample-averaged quantity, it gives little insight into the probability distribution of the number of adsorbed virions for an individual aerosol. Under the reasonable *a priori* assumption that adsorption of an individual virion by an aerosol is an independent random event, the conditional probability of an aerosol with at least one adsorbed aerosol carrying two or more virions is negligible. However, this assumption may be incorrect if there are physical mechanisms that endow a small number of aerosols with a large number of virions, while leaving the rest of the aerosols without virions. In an older study, artificially generated aerosols with adsorbed adenovirus virions were individually resolved with electron microscopy.[47] It was found that the vast majority (67%) of aerosol particles had only one virion, 11% had two virions, *etc.* Overall, it appears to be most likely that each infectious aerosol carries one to a few SARS-CoV-2 virions. A recent review of the soft matter science of COVID-19 broadly concurs with the analysis here.[48]

Generation and Morphology of Infectious Aerosols. Conceptually, we can distinguish several possible modes of association between virions and aerosols. For liquid aerosols, virions could be encapsulated within the aerosol or adsorbed at the aerosol surface. For solid aerosols, virions could be adsorbed to the aerosol surface or, if the aerosol is porous, contained within the aerosol structure. Moreover, the prevailing mode of association is clearly influenced by the biophysical process that generates the infectious aerosol.

Exhalation from infected individuals is obviously the most important process for generation of aerosols laden with SARS-CoV-2 virions. Coughing, sneezing, breathing, and human speech can produce liquid droplets with a broad size range, from <0.8 to 10 μm.[49,50] The droplets thus generated can contain virions, along with salts, biopolymers, and other biomolecules. Upon exposure to air, the fate of a droplet depends on its size and ambient conditions, especially RH. It is commonly assumed that large droplets (>5 μm) will quickly sediment to the ground, while smaller droplets (*i.e.*, aerosols) will remain aloft for a long period. Figure 1a shows a high-speed image of a sneeze; large droplets with ballistic trajectories are clearly visible (green), while a moist and buoyant "puff" (red) carries small droplets (discussed in detail below).[51] Aerosols in the size range between 0.5 and 5 μm are known to be the most breathable fraction of all aerosols (see Dispersion of Bioaerosols in Air for details).

It should be noted that droplet size is a dynamic quantity, as expelled droplets will start to evaporate if the ambient RH is

https://dx.doi.org/10.1021/acsnano.0c08484
ACS Nano 2020, 14, 16502–16524

<100%.[52] This will reduce the size of droplets, prolonging their time in air. The droplet settling time therefore largely depends on initial size and RH.[53] Since the pioneering work of Maxwell in 1877, many studies have sought to model, using continuum microscopic theory and numerical simulations, the coupled heat and mass fluxes in the vicinity of an evaporating droplet as well as the changing size of the droplet.[54−60] The coupling of the two fluxes through the latent heat and the moving boundary condition makes this a challenging problem in transport theory.[61] To simplify the modeling, various assumptions are commonly made, for example, that the droplet radius can be regarded as quasi-static or stationary for determination of the instantaneous heat and mass fluxes and that the surface of the droplet is in thermodynamic equilibrium. Recently, the problem of droplet evaporation has received fresh impetus from the COVID-19 pandemic; for instance, it was recently estimated that at 50% RH, droplets with the initial size smaller than 40 μm, released from a typical human height, will dry out before hitting the ground.[62]

Droplets that dry out in air produce solid residues, or "droplet nuclei," as shown schematically in Figure 1b.[63] Owing to their small size, these dry particles can potentially remain aloft for a long time. Using an aerodynamic particle sizer for droplets produced by coughing, Yang *et al.* determined that the dry nuclei size distribution peaked at 1 μm, consistent with a much earlier work from Duguid.[50,64] Drying of the droplet can potentially lead to gelation of mucin and other proteins contained in the droplet, and virions may be contained within the gel network.[65] We are not aware of any attempt to directly image droplet nuclei obtained from air in order to determine their morphology or microstructure. For instance, it would be useful to know whether virions are typically contained within droplet nuclei or are carried as surface adsorbates. However, there have been some experimental studies of the drying of model virus-laden solutions that were aerosolized and deposited on solid surfaces. In one such study, Vejerano and Marr determined *via* fluorescence microscopy that phi6 virions, used as a surrogate for influenza, were homogeneously dispersed within desiccated droplets (Figure 1c).[65] In another such study, three phi6-laden solutions—saliva, SM buffer, and water—were deposited on a surface and left to dry. Interestingly, the virions in saliva exhibited the greatest viability after 14 h, even though the saliva droplets completely evaporated in that time for all tested RH conditions, leaving a thin dry deposit. It was hypothesized that biopolymers in saliva may enhance virion survival.[66] Necessarily, these studies give little information on the interaction of virions and aerosols of comparable, that is, submicron, size. However, based on experimental and simulation studies involving nanoparticles and virions, it is plausible that SARS-CoV-2 virions and nanoaerosols bind to form a loose cluster.[47,67,68] For instance, the Cyro-TEM image in Figure 1d provides evidence of binding between vesicular stomatitis virions and small nanoparticles. Recently, this conceptual model of SARS-CoV-2 virions adsorbed to "carrier" nanoaerosols has motivated the development of nanofiber filters for capture and filtration of ambient nanoaerosols.[69]

Infectious aerosols can also be generated by medical procedures, such as intubation,[70] and even by flushing a toilet containing infectious material.[71] The relevance of these other mechanisms to COVID-19 transmission is poorly understood, but could easily be related to the superspreading events listed in the Introduction.

Dispersion of Bioaerosols in Air. The dispersion of aerosols has a strong dependence on ambient airflow, even when the aerosols are released only meters away from the ground, as in human exhalation or in medical procedures. As a reasonable first approximation, aerosols can be regarded as "point-like" or passive tracer particles that simply follow fluid pathlines. (Recall that a streamline is a curve tangent to the flow field at a particular moment in time, while a pathline is the trajectory followed by an individual parcel of fluid.) Thus, significant effort has been invested in understanding air flow in complex geometries characteristic of interior and exterior built environments. Meter-scale air flows in these environments are typically turbulent. Moreover, temperature variations (*e.g.*, induced by operation of medical devices or the heat output of human beings) can drive the natural convection of air.

Due to the complexity of the governing physics, computational fluid dynamics (CFD) packages like Fluent or Comsol are typically used to solve the energy equation (for the air temperature) and the Navier−Stokes equations (for the air velocity) in a meshed spatial domain.[72]

Direct numerical simulation (DNS) of the Navier−Stokes equations is usually computational prohibitive, requiring an approximate approach. One such approach is to consider the Reynolds-averaged Navier−Stokes (RANS) equations. These equations arise from decomposition of the Navier−Stokes equations into time-averaged and fluctuating components and subsequent time averaging of the equations. As a result, one obtains equations without an explicit time derivative, but with a new contribution to the fluid stress, the Reynolds stress. This stress is not known *a priori*, as it represents fluctuating components; one must choose a model (or "closure") for the Reynolds stress, such as the k-epsilon model. Another approximate approach, distinct from RANS, is large eddy simulation (LES). A recent paper by Blocken discusses the relative advantages of RANS and LES in modeling interior air flows.[73]

As an example of CFD used to model bioaerosol dispersion, Buchanan and Dunn-Rankin considered an operating room with heat generated by personnel and medical devices, which were meshed as solid objects.[74] They used Fluent to solve the energy balance equation and the RANS equations with k-epsilon closure. Aerosol particles were assumed to have velocities equal to the local air flow velocity, plus a stochastic component to model the effect of air flow velocity fluctuations. In another study, Li *et al.* considered a SARS superspreading event in a Hong Kong hospital ward, in which one patient infected 138 other patients, visitors, and medical personnel.[75] Airborne transmission was suspected in this event. Accordingly, the study combined inspections and measurements of the on-site ventilation system, some limited on-site experimental measurements of aerosol dispersion, and CFD modeling of the ventilation and air flow. In their CFD modeling, they included convection due to heat from patients, lighting, and heating systems and meshed the detailed geometry of the ward. Patients were included as rectangular prisms, and bioaerosols were assumed to disperse as passive tracers. The simulated aerosol distribution displayed reasonable agreement with measured concentrations.

In these single-particle models, one can obtain some additional realism without much additional model complexity by incorporating particle inertia. Specifically, one can add a differential equation for the particle velocity, allowing a particle to exhibit relative motion with respect to a background flow

https://dx.doi.org/10.1021/acsnano.0c08484
ACS Nano 2020, 14, 16502−16524

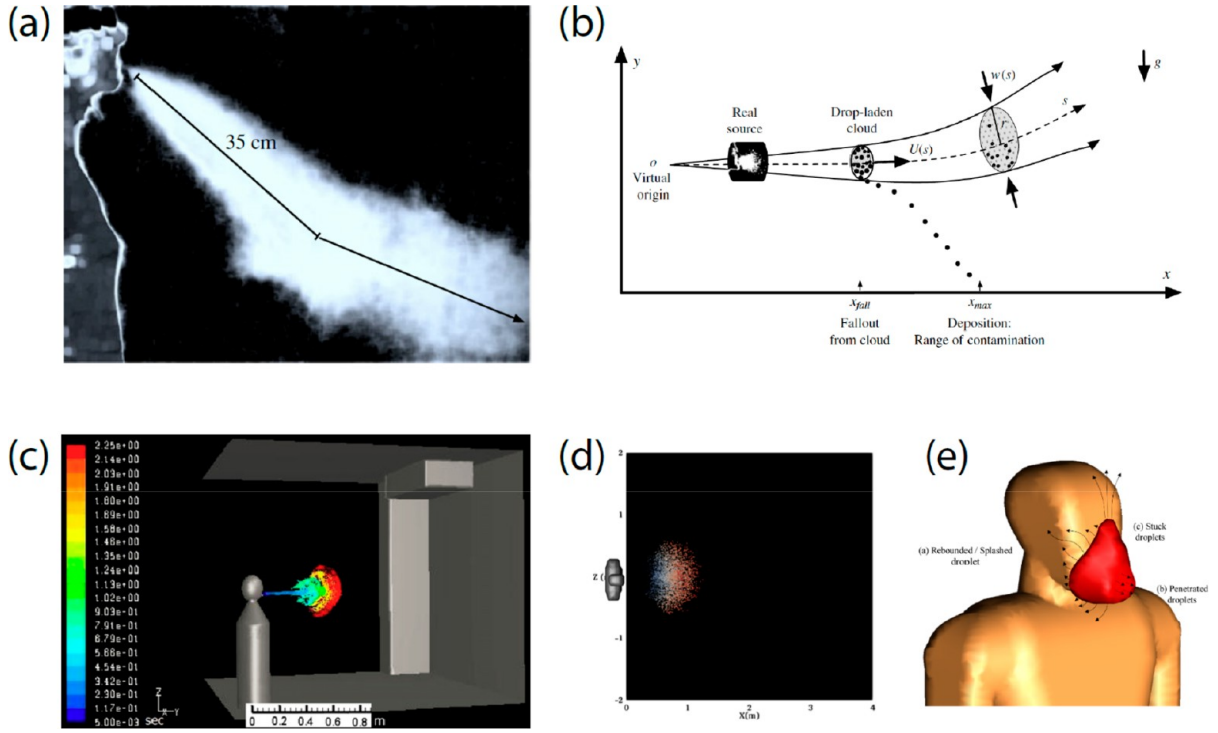

Figure 2. (a) A "puff" emitted from a human mouth during sneezing, imaged with a high-speed camera. Adapted with permission from ref 82. Copyright 2014 Cambridge University Press. (b) Schematic illustration of the trajectory of a cough or sneeze cloud. The trajectory has an upward curvature due to buoyancy. Droplets fall out of the cloud, contaminating surfaces. Adapted with permission from ref 82. Copyright 2014 Cambridge University Press. (c) CFD simulation of particles emitted from the mouth of meshed "mannequin," shown 2.25 s after a cough. Particles are colored by residence time in the atmosphere. Adapted with permission from ref 85. Copyright 2011 Elsevier. (d) Pattern of droplet deposition after sneezing, obtained by CFD simulations. In this case, the sneeze velocity was 6.3 m/s, and the droplet initial size distribution ranged from 40 to 980 μm with an average diameter of 540 μm, that is, outside of the aerosol range. Colors indicate the diameter of the deposited droplet, from 40 μm (deep blue) to 980 μm (deep red). In this case, and perhaps surprisingly, droplets that deposit close to the source are smaller than those that deposit farther away, suggesting the importance of droplet inertia in determining the pattern for larger droplets. In general, features of the deposition pattern are sensitive to droplet size distribution, initial velocity, and other parameters. Adapted with permission from ref 86. Copyright 2020 AIP Publishing. (e) Schematic illustration of different modes of interaction between droplets and a face mask. Adapted with permission from ref 86. Copyright 2020 AIP Publishing.

field. Particle density is also easily incorporated. Although the governing equations for particle motion are simple, tracers with inertia can have rich physics, even from a fundamental point of view. For instance, Vilela and Motter considered heavy inertial tracers in model open background flows.[76] Despite the expectation that aerosols can escape open flows in finite time, they found that the presence of vortices in the background flow can lead to permanent trapping of the aerosols. Concerning CFD of droplet dispersion in ventilated rooms, Sun and Ji modeled droplets produced by coughing as heavy tracers with inertia and simultaneously solved differential equations for the mass and energy fluxes from the evaporating droplets.[77] The background flow in a meshed model ventilated room was solved with RANS.

There may be other physical effects, microscopic in origin, that cause particles to move relative to background flows. For instance, phoretic forces in concentration and/or temperature gradients could contribute to particle motion. Although some recent papers have considered phoretic effects in turbulent flows,[78,79] this topic is largely unexplored, and further work is needed to assess the relevance of phoresis in the specific context of air flows. The effect of nonspherical aerosol shape in turbulent flows is also a vigorous area of research.[80] Concerning Brownian motion of aerosols, one study has concluded that it is generally dominated by turbulent diffusion, that is, random motion from turbulent velocity fluctuations.[81]

So far, our discussion has considered the motion of single droplets in ambient air flows determined by room ventilation and temperature conditions. However, recent research has shown that, during sneezing and coughing, droplets are emitted in turbulent gas clouds, that is, discrete puffs or continuously emitted jets.[82,83] (More precisely, jets are continuously provided momentum by the emitter, while puffs have a conserved quantity of momentum.) The momentum, temperature, humidity, and chemical composition of the cloud can have a significant effect on droplet trajectories and evaporation dynamics.[25] The RH in a cloud is typically much higher (~85%) than the RH in interior spaces (~40%, although this can vary according to season and climate), prolonging droplet lifetime. Moreover, the infectivity of respiratory viruses is apparently lower under conditions of intermediate ambient RH (*i.e.*, 40−60%) than high ambient RH (>60%); the humid microenvironment provided by the cloud could potentially promote infectivity before it disperses.[33,84] Concerning temperature, the jet or puff emitted from the body will generally be warmer than ambient conditions, providing some initial positive buoyancy to the cloud. Bourouiba *et al.* used high-speed photography to directly image puffs, including suspended droplets, emitted by adult human subjects during coughing and sneezing events (Figure 2a).[82] Large droplets were

https://dx.doi.org/10.1021/acsnano.0c08484
ACS Nano 2020, 14, 16502−16524

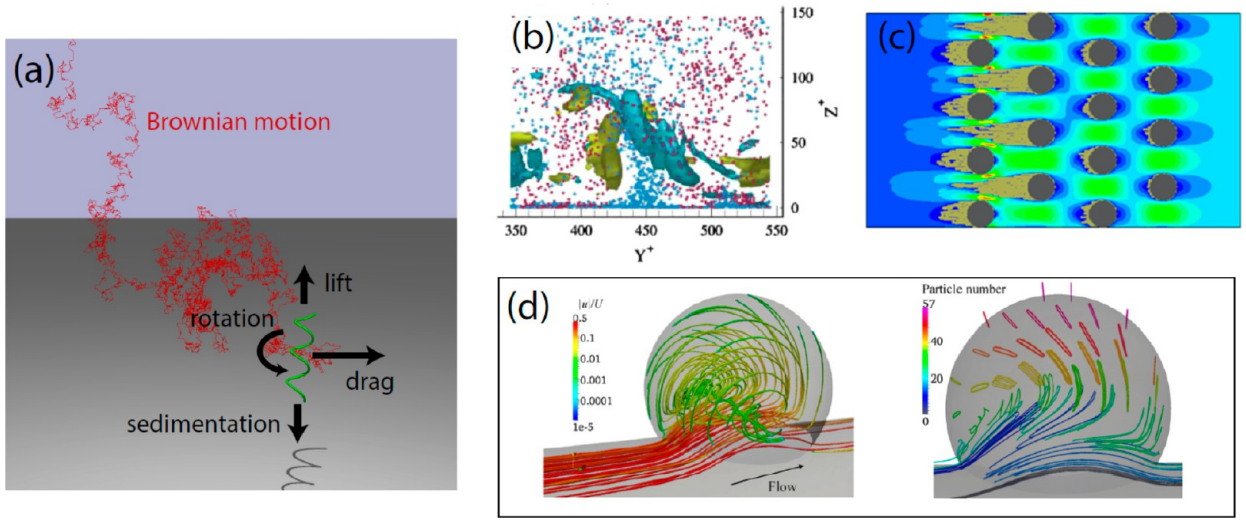

Figure 3. (a) Schematic illustration of the deposition of an aerosol particle onto a surface. The particle is exposed to Brownian, gravitational, viscous drag, and/or phoretic forces. The effects of inertia and nonspherical shape can lead to lift forces on the particle. Complex particle trajectories can result from the interplay of these various forces. (b) Particles in confined turbulent flows can segregate and exhibit coherent motions as they are carried by turbulent flow structures. Purple dots represent particles moving toward the wall located at $z^+ = 0$, and blue dots represent particles moving away from the wall. The green isosurface identifies a counterclockwise rotating vortex, while the blue isosurface identifies a clockwise rotating vortex. The mean flow is directed out of the page. Adapted with permission from ref 93. Copyright 2009 Elsevier. (c) Deposition of aerosols onto a fiber array in the inertial impaction flow regime. Air containing aerosols flows continuously from left to right through the array. Large black circles indicate fiber locations. Small gray circles represent deposited aerosol particles. The magnitude of the flow velocity is shown *via* the color field; warmer colors indicate faster flow. The flow field (magnitude shown by the color field) was obtained with the LBM. Adapted with permission from ref 110. Copyright 2013 Elsevier. (d) Flow streamlines (left panel) and particle trajectories (right panel) in a model alveolus during tidal breathing. Adapted with permission from ref 102. Copyright 2013 Elsevier.

observed to move ballistically, with little effect from the surrounding cloud, while smaller droplets (visible as mist) tended to move with the cloud over long distances. Puff clouds initially evolved as cones with some upward curvature due to buoyancy, consistent with an established model of self-similar growth of turbulent jets by entrainment of ambient fluid. An analogue experiment involving the injection of fresh water into salty water allowed the authors to probe the crossover between jet-like and puff-like cloud dynamics. Moreover, a theoretical model was developed to describe fallout of droplets as the puff entrains fluid and decelerates (Figure 2b).

While Bourouiba *et al.* used analytical modeling, CFD modeling can be extended to include turbulent jets and puffs ejected during coughing and sneezing. Redrow *et al.* used CFD to model the dispersion of particles in an initially buoyant jet emitted from the mouth of a meshed "mannequin", using initial conditions determined from cough flow rate data from the National Institute of Occupational Safety and Health (NIOSH).[85] They found that the maximal particle concentration appeared 0.65 m from the mouth of the mannequin (Figure 2c). In the same work, Redrow *et al.* sought to extend droplet evaporation models to account for the local temperature and chemical composition of ejected gas clouds. A similar study was recently carried out by Pendar and Pascoa, motivated by the need to determine social distancing guidelines in the context of COVID-19 (Figure 2d,e).[86] Indeed, CDC guidelines, including the familiar six-foot rule, are still based on the 1930s-era concept of an isolated respiratory droplet settling under gravity, despite the wealth of contemporary literature reviewed above. In a recent work, several investigators in the airborne transmission community have sought to develop an integrated framework that consolidates recent insights concerning ejection, dispersion, and inhalation of respiratory droplets, and which can provide concrete guidance for social distancing (in both space and time) *via* simple model equations.[51]

Modeling of Aerosol Deposition onto Surfaces. Infectious aerosols in the atmosphere can deposit onto surfaces as fomite contaminants. Physical contact of a potential host with fomites can lead to infection hours or even days after deposition.[43] Moreover, infectious aerosols that are inhaled must travel through lung airways and ultimately deposit on an interior surface in order to transmit virions (for details see Future Directions in Modeling Aerosol Dispersion and Deposition). In both scenarios, an aerosol and associated virions must move in near-surface fluid flow, subject to sedimentation, diffusion, phoretic forces, and other effects, and adsorb to the surface, as shown schematically in Figure 3a. An understanding of this physical process could facilitate development of mitigation strategies, for example, surface coatings that hinder deposition or reduce the viability of adsorbed virions.

Empirically, it is well-established that fluid flows tend to "stick" to solid surfaces, that is, the fluid velocity obeys a no-slip boundary condition on surfaces. Accordingly, air flow will slow down in the vicinity of surfaces, especially within surface boundary layers. Within boundary layers, which include the laminar sublayer of turbulent flow, the flow can be regarded as viscous. Accordingly, the physics of deposition can be significantly different from the physics of dispersion in the atmosphere. For instance, Brownian diffusion may play a significant role near surfaces even when it is irrelevant in the bulk fluid. A point-like description of the particle may no longer be valid, as the near-surface flow may vary on length scales comparable to the particle size. Moreover, the inertia of the fluid and/or of the particle can potentially be disregarded in these regions, owing to the reduction of the flow speed and,

https://dx.doi.org/10.1021/acsnano.0c08484
ACS Nano 2020, 14, 16502−16524

consequently, of the fluid and particle Reynolds numbers. In the remainder of this section, we review some of the literature on modeling deposition of aerosols.

Much of the groundwork on deposition in the viscous sublayer of turbulent flow, similar to what would be expected in fomite deposition, was laid by McLaughlin, Ahmadi, and co-workers.[87,88] An influential early model considered the deposition of a spherical particle *via* Brownian dynamics.[87] The mean background flow was modeled as a linear shear profile. The dynamics of the particle was modeled with a Langevin equation involving an inertial term, viscous drag terms, and a Brownian fluctuating term. The effect of turbulent fluctuations was crudely modeled with a wall-normal contribution to the flow velocity that varied quadratically with distance from the wall. The authors found that Brownian motion dominated the deposition process close to the wall.

We highlight this particular model as capturing the most basic physical effects affecting deposition and as a point of departure for development of more realistic models. Limitations of the model include the neglect of aerodynamic (*i.e.*, fluid-mediated) interactions of the particle with the wall; these interactions lead to variation of the drag coefficient and noise term with distance from the wall.[89] The particle is considered to be point-like, that is, gradients in the background flow velocity in the vicinity of the particle do not affect the particle velocity. Phoretic, electrostatic, and other forces are not included. Inertia of the fluid, which can give rise to wall-normal forces, is neglected. The particle shape is assumed to be spherical, and the background flow is severely approximated. Finally, if the virion size is comparable to the aerosol size (recalling the earlier discussion of relative size), the multibody dynamics of aerosol and associated virion or virions must be considered.

Many of these limitations were addressed in subsequent papers that also worked within the Brownian dynamics framework. For instance, Fan and Ahmadi considered deposition of ellipsoidal particles.[90] The model includes the anisotropic drag on the particle, that is, the fact that drag is smaller for motion along the major axis than for motion along a minor axis. The particle orientation evolves according to coupled Langevin equations, with the orientation represented with quaternions. A term representing the shear-induced lift force (which arises from fluid inertia) is included in the Langevin equation. This addition is somewhat *ad hoc*, in the sense that the lift force is represented by a phenomenological term in force balance equations and does not emerge from a solution of the dynamics of the suspending fluid.

With the growth of computing power, a recent trend is to simulate the background flow in the viscous sublayer with CFD by DNS. For instance, Zhang and Ahmadi used a pseudospectral DNS method to generate time-dependent instantaneous velocity fields in vertical and horizontal ducts.[91] The motion of a spherical aerosol was again modeled with a Langevin equation, in this case with a Reynolds number-dependent drag term. Another paper from the same group combined CFD simulation of velocity and temperature fields with a model for thermophoretic force on a sphere.[92] Marchioli, Soldati, and co-workers have also been very active in applying DNS, especially pseudospectral methods, to aerosol deposition.[93] In particular, their work highlights the key role of coherent flow structures like quasi-streamwise vortices in segregating and trapping aerosols, depositing them onto walls, and re-entraining them from walls (Figure 3b).

In the specific context of bioaerosol inhalation and infection, various studies have addressed aerosol motion and deposition in the confined spaces of lung alveoli.[94−100] Small aerosols (<1−2 μm) preferentially deposit in alveoli (see Future Directions in Modeling Aerosol Dispersion and Deposition for details).[101] Flows in these spaces generally possess low Reynolds numbers, with the Reynolds number varying characteristically between 0.01 and 10.[102] Alveoli expand and contract during breathing, making the flow and confining geometry time dependent. Balashazy *et al.* modeled this flow analytically using a superposition of model uniform and radial flow components in an idealized hemispherical alveolus geometry. Aerosol trajectories were calculated *via* Brownian dynamics and included the effects of particle inertia, Brownian motion, and sedimentation. They found that the orientation of the alveolus with respect to gravity can affect the deposition efficiency for larger aerosols.[97] Similarly, Haber *et al.* applied a mixed numerical and analytical approach to solve for the flow in a model alveolus in the shape of a truncated spherical cavity.[94] Additionally, they solved for the deterministic trajectories of massless particles (*i.e.*, passive tracers) and found that they followed complex, chaotic, and effectively stochastic pathlines. Similar results for flow streamlines and particle trajectories were obtained by Sznitman, as shown in Figure 3d.[102] A comprehensive review of aerosol delivery in the respiratory tract is provided by Longest and Holbrook.[103]

Future Directions in Modeling Aerosol Dispersion and Deposition. We suggest two promising directions for simulation of aerosol deposition. The Brownian dynamics method can be combined with the boundary element method (BEM) for the solution of Stokes flow (the viscous limit of the Navier−Stokes equations) in complex confined geometries. Specifically, the BEM can capture the aerodynamic effect of complex particle shape and aerodynamic interactions with confining surfaces.[104] A recent work by Gubbiotti *et al.* demonstrates how to consistently model fluctuating Brownian motion in confinement, suggesting combination of this Brownian dynamics approach with the BEM.[105] Since the particle surface is meshed in the BEM, anisotropic and "patchy" or surface-heterogeneous forces can be included in a straightforward manner. The multibody dynamics of several particles, representing an aerosol and associated virions, can be modeled in this approach. However, the BEM is most suitable to linear partial differential equations; for instance, it is not straightforward to include the effect of fluid inertia. Another promising approach is the lattice Boltzmann method (LBM) with fluid−structure interaction between the fluid (modeled as an LBM fluid) and moving particles.[106,107] Here, the effect of fluid inertia naturally arises from the underlying fluid lattice dynamics. The LBM has been successfully applied to airflow analysis in the alveolar region of the lung,[108] electrophoretic deposition of aerosols onto a sensor surface,[109] and filtration of aerosols by fiber arrays (such as in N95 masks),[110] as shown in Figure 3c.

AEROSOL DEPOSITION IN THE LUNG

Regional Deposition in the Lung. The respiratory system is the first and primary body region affected by SARS-CoV-2. Inhaled virus-laden aerosols deposit in different regions of the respiratory system, depending on the physicochemical properties of the aerosols, including their aerodynamic size, density, shape, charge, hydrophobicity, and hygroscopicity.[111] Among these influencing factors, the aerodynamic size plays a

https://dx.doi.org/10.1021/acsnano.0c08484
ACS Nano 2020, 14, 16502−16524

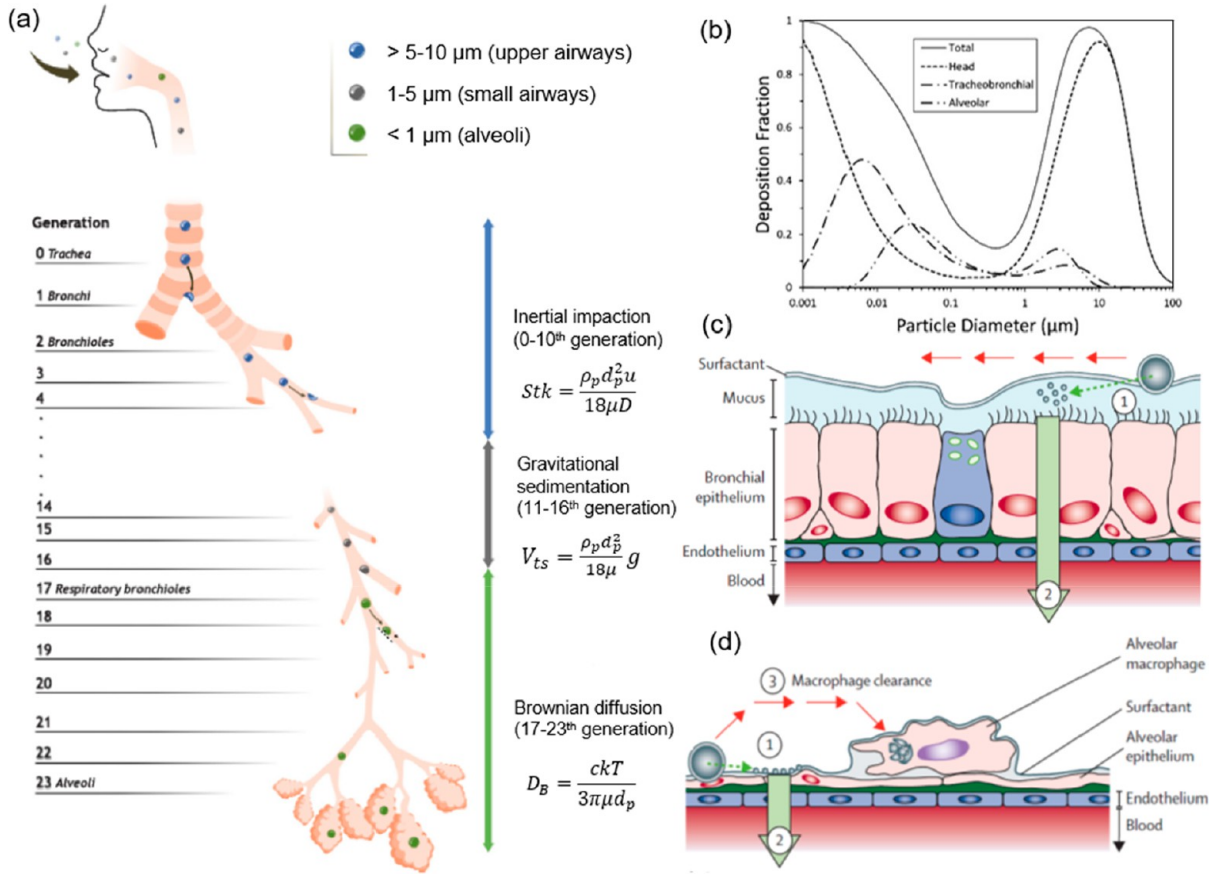

Figure 4. Size-dependent regional deposition and clearance of inhaled aerosols in the lung. (a) Branched architecture of the lung and mechanisms of regional deposition of aerosols. Large aerosols >5−10 μm primarily deposit in the nasopharynx and the tracheobronchial region of the lungs (first 10 generations) where their deposition is affected by inertial impaction. Medium-sized aerosols between 1 and 5 μm mostly deposit in small airways (11th−16th generations) where the governing mechanism is gravitational sedimentation. Small aerosols <1 μm can penetrate into the alveolar region where Brownian diffusion controls their motion. Adapted with permission from ref 114. Copyright 2019 Elsevier. (b) Mathematical model of particle deposition in the whole lung (total), nasopharynx and larynx (head), tracheobronchial airways, and alveolar region of healthy adults *via* nasal breathing with a flow rate of 250 mL/s. Adapted with permission from ref 113. Copyright 1999 John Wiley & Sons. (c, d) Clearance mechanisms of inhaled aerosols. Large aerosols >5 μm are excreted from upper airways with mucociliary escalator (c), while small aerosols <5 μm are cleared from alveoli with macrophage phagocytosis (d). Adapted with permission from ref 122. Copyright 2013 Elsevier.

predominant role in determining the regional deposition of inhaled aerosols (Figure 4b).[112,113]

As shown in Figure 4a, the lung, a key infection site, features a branched architecture that consists of 23 generations of dichotomous branching, from the relatively thick trachea (generation 0), with an average diameter of 15−25 mm, to small airways with diameters of <2 mm, ending up with 300−600 million of terminal alveoli (generation 23), with an average diameter of only 200 μm per alveolus.[114,115] The primary mechanisms of aerosol deposition in the lung include inertial impaction, gravitational sedimentation, and Brownian diffusion as well as, to a lesser extent, interception (applied to elongated aerosols such as fibers) and electrostatic precipitation (applied to charged aerosols).[112,114,116,117]

Inertial impaction mainly affects large aerosols >5−10 μm. These large aerosols primarily deposit in the nasopharynx and the tracheobronchial region of the lung (first 10 generations) where the air flow rate is high and the flow condition is predominantly turbulent. The degree of particle deposition by inertial impaction is quantified by the dimensionless Stokes number (Stk), defined by $\mathrm{Stk} = \frac{\rho_p d_p^2 u}{18\mu D}$, where, ρ_p and d_p are the density and aerodynamic diameter of the airborne particles, respectively, u and μ are the mean velocity and dynamic viscosity of the air flow, respectively, and D is the characteristic diameter of the airway.

Gravitational sedimentation mainly affects medium-sized aerosols between 1 and 5 μm. These medium-sized aerosols mostly deposit in small airways (11th−16th generations) where the flow rate is low and the particles have a relatively long retention time in this region. The terminal settling velocity (V_{ts}) of the particles is expressed by $V_{ts} = \frac{\rho_p d_p^2}{18\mu} g$, where, g is the gravitational acceleration.

Brownian diffusion is the mechanism that controls the motion of small aerosols mainly <1 μm in diameter. These small aerosols can penetrate into the alveolar region where the air flow rate can be approximated as negligible. Deposition by Brownian diffusion is proportional to the Brownian diffusion coefficient (D_B) defined by $D_B = \frac{ckT}{3\pi\mu d_p}$, where k is Boltzmann's constant, T is the absolute temperature, and c is the Cunningham correction factor.

https://dx.doi.org/10.1021/acsnano.0c08484
ACS Nano 2020, 14, 16502−16524

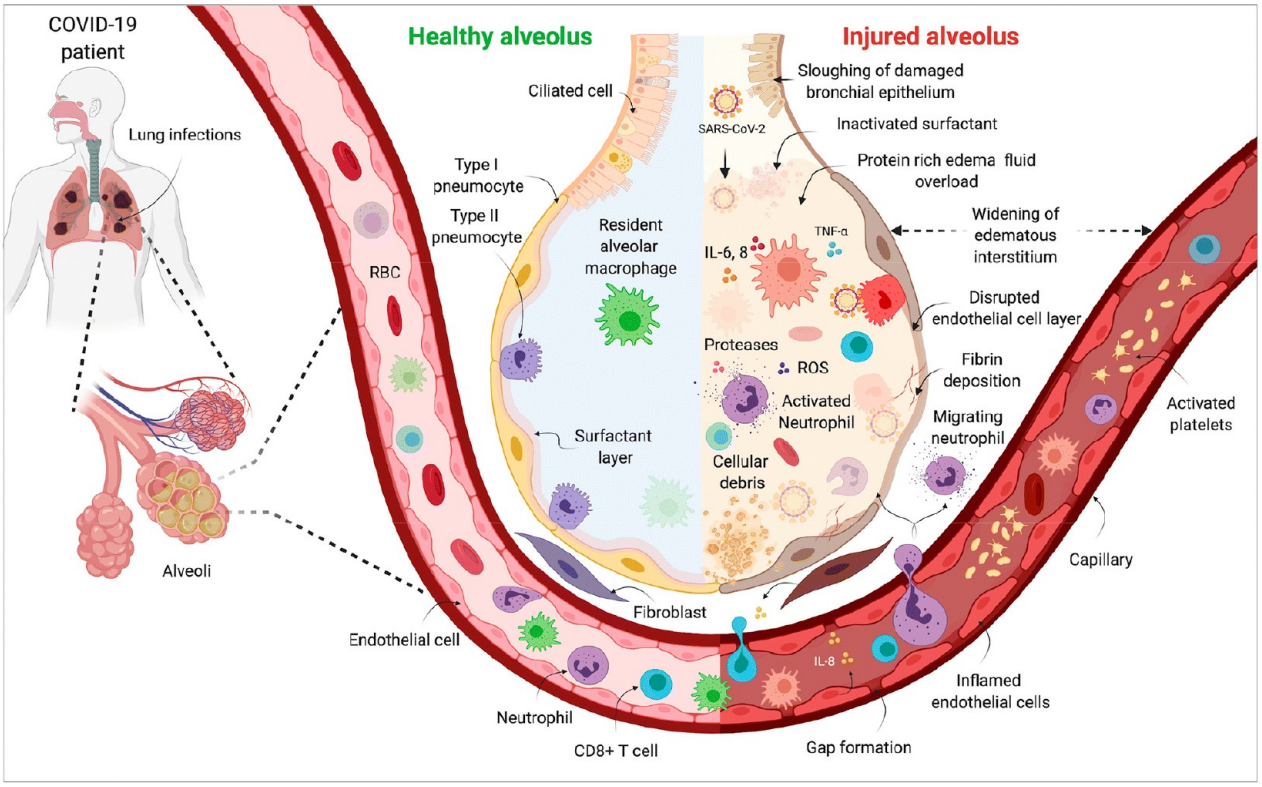

Figure 5. COVID-19-induced ARDS. SARS-CoV-2 attacks the surfactant-producing type II alveolar epithelial cells *via* ACE2 receptors expressed on the surface of type II cells. Disruption of the PS system leads to alveolar instability, lung flooding, and respiratory failure. In addition, ARDS generates a hyperactive immune response, localizing neutrophils and increasing cytokine release, which leads to the accumulation of reactive oxygen species, cell debris, and proteases. Adapted with permission from ref 131. Copyright 2020 Springer Nature.

Depending on their specific deposition regions, inhaled aerosols experience two different clearance mechanisms in the lung. Aerosols larger than 5 μm, including most respiratory droplets, are deposited in the upper regions of the respiratory tract, from which they are removed by the mucociliary escalator and eventually spit out or swallowed (Figure 4c).[118] Mucociliary clearance is regulated by a dual-layered airway surface liquid composed of a ~10 μm-thick aqueous periciliary liquid (PCL) plus a 10−70 μm-thick viscoelastic mucus gel layer atop the PCL.[119,120] This clearance mechanism is chemically nonspecific and highly efficient, with 80−90% of inhaled aerosols being excreted from the lung within 24 h.[121,122] In contrast, aerosols smaller than 5 μm, especially those smaller than 3 μm,[112] are capable of penetrating to the distal alveolar regions of the lung, at which the primary clearance mechanism is macrophage clearance with the assistance of the immunological surfactant proteins (Figure 4d).[122−124] Macrophage clearance is found to be most effective for aerosols in the size range 0.5 and 5 μm,[125] which happens to be the most breathable fraction of all aerosols.[112,122]

Interaction with the Pulmonary Surfactant Film. In contrast to direct and fomite transmissions, by which SARS-CoV-2 first infects the nasal cavity, replicates itself in the upper airways, and eventually propagates into the lung periphery,[126] SARS-CoV-2 transmission mediated by aerosols may directly infect the lung interior,[20,127] thus leading to a rapid onset of the most severe third-phase alveolar infection of COVID-19.[128,129] As illustrated in Figure 5, once reaching the alveolar regions, SARS-CoV-2 attacks both type I and type II alveolar epithelial cells, promotes lung flooding, and causes the life-threatening acute respiratory distress syndrome (ARDS).[130−132] SARS-CoV-2 attacks cells *via* the angiotensin-converting enzyme 2 (ACE2) receptor (see Pulmonary Surfactant Biomolecular Corona for detailed mechanisms of virus interaction with ACE2 receptors),[133] which is highly expressed on the surface of type II cells.[134] Among the most important physiological functions of these cells is the production of PS, a lipid−protein complex that lines the entire air−water surface of alveoli as a thin film.[135] It is composed of mostly lipids (~90% by weight) and four surfactant associated proteins, that is, SP-A, B, C, and D (~10% by weight).[135] A closer evaluation of the lipid portion of PS reveals that the majority of the lipids are phospholipids that contribute to its high surface activity (*i.e.*, the ability to reduce surface tension).[136,137] SP-B and SP-C are hydrophobic proteins embedded in the phospholipid matrix that work with phospholipids to achieve low surface tensions during normal tidal breathing.[138] SP-A and SP-D are hydrophilic proteins that assist in innate immune responses, including macrophage clearance,[139] although SP-D is only partially associated with the PS membranes.[140]

The PS film serves two major physiological functions. The first function of the PS is innate immunity, that is, serving as the initial alveolocapillary barrier and first-line host defense against aerosols and pathogens that reach the deep lung.[141,142] The immunological function of the PS is mostly regulated by the two hydrophilic surfactant proteins, SP-A and SP-D. It has been reported that macrophage phagocytosis of nanoparticles was triggered by SP-A.[124] In addition, SP-D bound to the spike protein of SARS-CoV triggered macrophage phagocytosis of the virus.[143] The second function of the PS is its biophysical function that allows for normal lung mechanics and prevents lung collapse by reducing the alveolar surface tension. With

https://dx.doi.org/10.1021/acsnano.0c08484
ACS Nano 2020, 14, 16502−16524

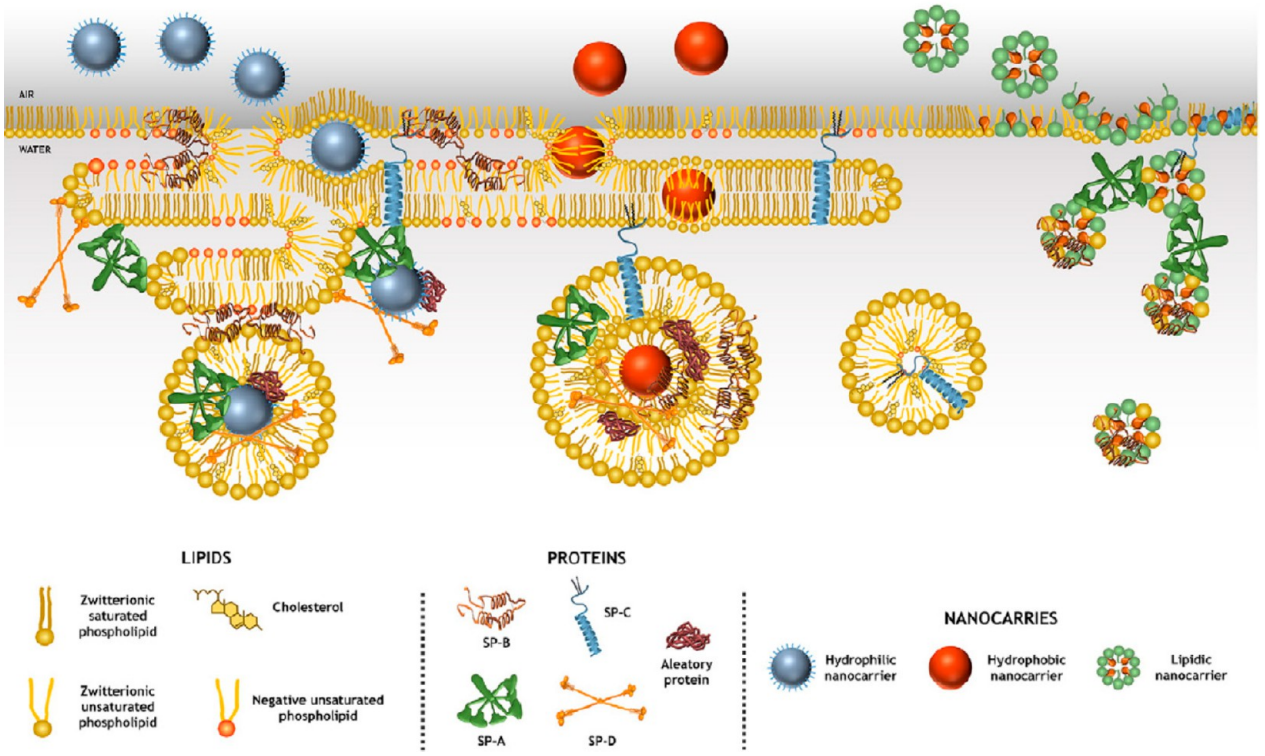

Figure 6. Interaction of hydrophobic and hydrophilic nanoparticles with the PS film. This cartoon illustrates how phospholipids, cholesterol, hydrophobic surfactant proteins (SP-B and SP-C), and hydrophilic surfactant proteins (SP-A and SP-D) may interact with nanoparticles, as regulated by their surface hydrophobicity. Adapted with permission from ref 142. Copyright 2017 Elsevier.

surface tension reduction to near-zero levels, inhalation−exhalation cycles are maintained at minimum mechanical energy expense.[135] Depending on their physicochemical properties, inhaled particles could interfere with the physiological function of PS *via* two major perspectives. First, particles may directly inhibit the biophysical function of the PS film at the air−water surface of alveoli (Figure 6).[144−146] By binding and denaturing hydrophobic surfactant proteins (SP-B and/or SP-C), particles cause surfactant inhibition, quantitatively measured by increasing surface tension and PS film compressibility during respiratory cycles,[146,147] thereby leading to alveolar collapse and respiratory failure, which is a major symptom of ARDS.[135] A wealth of *in vitro* and *in vivo* studies have demonstrated that the biophysical function of PS can be inhibited by various particles, including nanoparticles,[144−148] nanoenabled sprays and drugs,[149,150] PM2.5,[151−153] and pathogens such as the H1N1 influenza virus.[154] Second, particles may interfere with PS metabolism and homeostasis in the alveolar hypophase. It was found that nanoparticles caused surfactant degradation from the more surface active large aggregates to less surface active small aggregates.[144] The poor surface activity of small aggregates is attributed, at least in part, to depletion and/or denaturation of the surfactant proteins, especially SP-B and/or SP-C, which are membrane associated proteins that promote vesicle fusion to form more surface active large aggregates.[155,156]

In COVID-19-induced ARDS, damage to type II cells inevitably compromises PS synthesis. The combination of activated macrophages and large numbers of neutrophils recruited to the lung could lead to seven times more phospholipid clearance than the normal lung.[157] This increased phospholipid clearance could, over time, lead to smaller pools of functional surfactant and hence further impair its biophysical function of reducing the alveolar surface tension.[157] Consequently, there is a strong rationale for using exogenous surfactant replacement as a supportive therapy to treat COVID-19 patients, especially those critically ill patients requiring mechanical ventilation. In a recent report of a small-scale clinical trial, intratracheal administration of Curosurf, a porcine surfactant preparation, to mechanically ventilated patients appeared to promote positive clinical outcomes in four out of five patients.[158]

Pulmonary Surfactant Biomolecular Corona. Upon contacting the alveolar lining fluid, nanoparticles immediately adsorb biomolecules to form the so-called PS biomolecular corona.[144,145,159] This PS corona formed on inhaled aerosols can be considered as a counterpart of the well-recognized protein corona formed on nanoparticles entering the bloodstream.[160−163] It is generally accepted that formation of the biomolecular corona is an entropy-driven process, in which the decrease in entropy of the adsorbed biomolecules is more than compensated for by the increase in entropy of the released water molecules.[160−163] Numerous studies have shown that it is the biophysicochemical properties of the biomolecular corona, rather than that of the pristine particles, that determines the biological identity of the particles entering the human body.[162] The PS corona determines the biodistribution, bioreactivity, biopersistence, retention, translocation, and clearance of inhaled particles.[164,165] Hence, it is important to better understand the effect of this PS biomolecular corona on virus-laden aerosols and how the PS corona affects cellular uptake and cytotoxicity of the virus-laden aerosols.

A number of *in vitro* studies have demonstrated the formation of PS corona on nanoparticles.[144−146,166] For example, preincubating various nanoparticles, for example, single-walled

https://dx.doi.org/10.1021/acsnano.0c08484
ACS Nano 2020, 14, 16502−16524

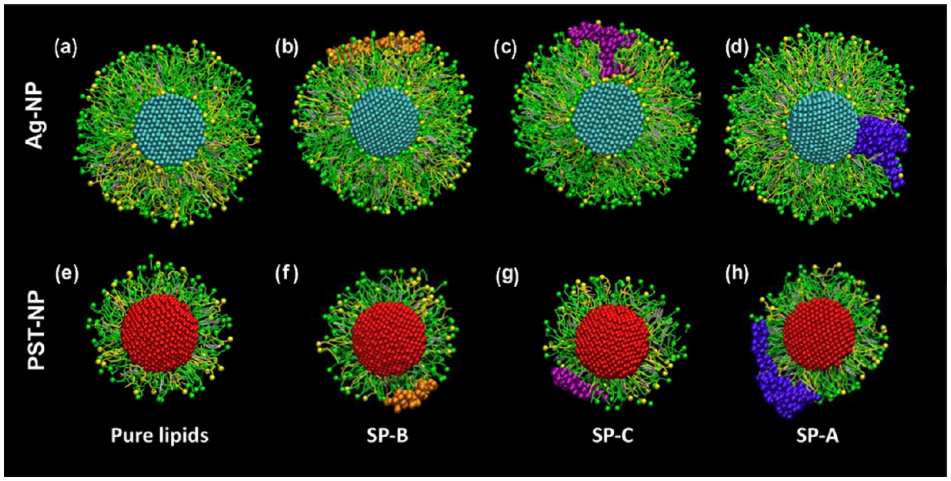

Figure 7. MD simulations of the chemical composition and molecular structure of the PS corona formed on two representative nanoparticles: (a–d) a hydrophilic silver nanoparticle (Ag-NP) and (e–h) a hydrophobic polystyrene nanoparticle (PST-NP). The Ag-NP and PST-NP are shown in cyan and red, respectively. Dipalmitoylphosphatidylcholine (DPPC) molecules are shown in green, palmitoyloleoylphosphatidylglycerol (POPG) in yellow, cholesterol in silver, SP-B in orange, SP-C in purple, and SP-A in violet. Adapted with permission from ref 159. Copyright 2017 American Chemical Society.

carbon nanotubes,[167] polystyrene,[168] and silica nanoparticles,[169] in PS-containing bronchoalveolar fluid significantly altered the particle uptake by alveolar epithelial cells and macrophages. The specific chemical composition and molecular conformation of the PS corona depend on the physicochemical characteristics of the particles, such as their size, shape, charge, hydrophobicity, and agglomeration state.[144−147,159,166] Among these properties, hydrophobicity of the nanoparticles appears to play a predominant role in affecting the PS corona (Figure 6). However, because of technical difficulties in determining the hydrophobicity of nanoparticles, there are only scarce studies that quantitatively evaluate the effect of particle hydrophobicity on PS biophysical properties[147] and corona formation.[159] A recent invention of an easy-to-use optical method that is capable of measuring the surface free energy of micro- and nanoparticles, as a quantitative measure of hydrophobicity, may be used for quantitatively evaluating the effects of particle hydrophobicity on the biomolecular corona.[170]

Other than direct experimentation, coarse-grained molecular dynamics (CGMD) simulations have been used to study the detailed chemical composition and molecular conformation of the PS biomolecular corona. Figure 7 shows the PS corona formed on two representative nanoparticles, that is, the hydrophilic silver nanoparticle and the hydrophobic polystyrene nanoparticle.[159] It is clear that the PS corona formed on both nanoparticles consists of a lipoprotein complex that contains both lipids and proteins. The specific structure of the corona and its molecular conformation are affected by the hydrophobicity of the nanoparticle, with a lipid bilayer formed on the hydrophilic silver nanoparticle and a lipid monolayer formed on the hydrophobic polystyrene nanoparticle. The two hydrophobic surfactant proteins, SP-B and SP-C, appear to mediate the formation of the corona by directly interacting with lipids in the corona, with SP-B orienting in parallel to the lipid bilayer and the helical fragment of SP-C adopting a transmembrane orientation. The hydrophilic SP-A was also found associated with the PS corona, mainly *via* its carbohydrate recognition domain, albeit to a lesser extent of association than SP-B and SP-C.

Although the detailed structure and composition of the PS biomolecular corona are yet to be discovered, both MD simulations and mass spectrometry studies suggest that this corona consists of primarily phospholipids,[167,171] hydrophobic surfactant proteins,[144,145] and hydrophilic surfactant proteins.[123,172,173] A fine balance between electrostatic and hydrophobic interactions may be involved in the formation of the PS biomolecular corona.[145] The PS corona provides the particles with a physicochemical barrier against the environment, reduces the hydrophobicity of the pristine particles, and enhances biorecognition of the particles.[159]

Future Directions in Understanding Aerosol Deposition in the Lung. Although plausible, direct clinical evidence for lung infection by virus-laden aerosols is still lacking. A common objection against the likelihood of aerosol transmission is the seemingly insufficient viral concentration to cause an infection, after individual airborne viral emissions in the form of a sneeze or a cough, or after continuous airborne viral emissions in the form of speaking or breathing. The aerosol volumes generated by an individual sneeze and cough are estimated at 1000 and 100 nL, respectively.[174] The aerosol volumes generated by continuous talking and breathing are estimated at 10 and 1 nL/min, respectively.[174] Given the estimated viral load of SARS-CoV-2 in saliva at 1000 virions per nL,[174] a COVID-19 patient could generate at least 1000 airborne SARS-CoV-2 virions per minute. This rough estimation is in general agreement with experimental measurements of airborne SARS-CoV-2 virions exhaled by COVID-19 patients.[27] After aerosol emission from the reservoir (*i.e.*, an infectious individual) and before aerosol deposition in the deep alveolar regions of a susceptible host, the viral concentration would be continuously diluted during aerosol transmission, decay, and nonspecific deposition.[175] Only a very small fraction of the virus-laden aerosols, likely those within the most breathable size range between 0.5 and 5 μm, may carry SARS-CoV-2 deep to the terminal alveoli. It is unclear if these amounts of virus are enough to cause lung infection. The infectious dose of SARS-CoV-2, that is, the average number of virions necessary to cause an infection for COVID-19, is still unknown, but it is estimated at ~1000 virions by analogy to influenza and other coronaviruses.[174] If so, there appears to be a high likelihood of airborne transmission of SARS-CoV-2, especially in scenarios involving

https://dx.doi.org/10.1021/acsnano.0c08484
ACS Nano 2020, 14, 16502−16524

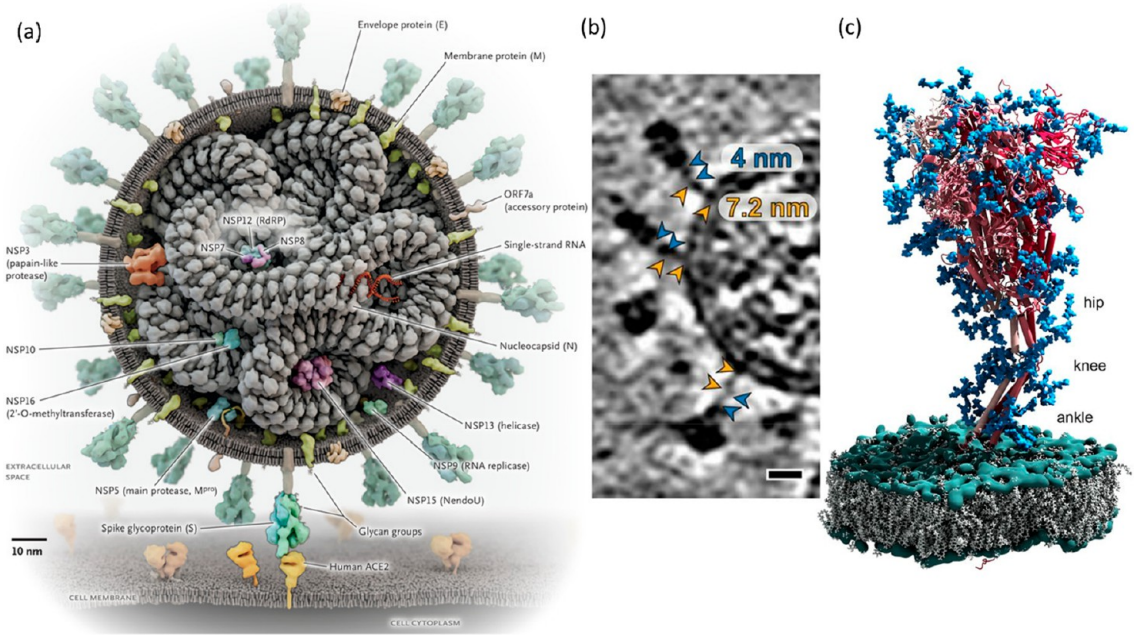

Figure 8. (a) Schematic of SARS-CoV-2 virion and its proteins. Adapted with permission from ref 212. Copyright 2020 Massachusetts Medical Society. (b) Cryo electron tomography of the virus. Adapted with permission from ref 182. Copyright 2020 American Association for the Advancement of Science. (c) Atomistic MD simulations of a fully glycosylated full-length S protein of SARS-CoV-2, embedded in a virial lipid membrane. The S protein is shown in red, N-glycosylation in blue, phosphates in green, and lipid membrane in gray. Each stalk has three flexible hinge structures, named the hip, knee, and ankle, that link the S protein to the viral membrane. Water and ions are omitted for clarity. Adapted with permission from ref 182. Copyright 2020 American Association for the Advancement of Science.

indoor environments, poor ventilation, prolonged exposure to events involving heavy breathing, or aerosol-generating medical procedures.

It is unknown how interactions with the PS system may affect the behavior of virus-laden aerosols in the lung. On the one hand, the PS biomolecular corona formed on aerosols reaching the alveolar regions would mediate macrophage clearance of these virus-laden aerosols and their interactions with the ACE2 receptor expressed on the surface of alveolar type II cells. On the other hand, injury of the surfactant-generating type II cells would worsen lung homeostasis and lead to ARDS symptoms such as alveolar flooding and leakage of the alveolar-capillary barrier, which would further induce surfactant inhibition. Hence, in spite of its failure in past ARDS trials, exogenous surfactant therapy may become beneficial for patients with COVID-19-induced ARDS, in which damage of the type II cells is an established pathogenesis.[129]

MOLECULAR INTERACTIONS OF SARS-COV-2 WITH THE ACE2 RECEPTOR

Modeling SARS-CoV-2 Spike Protein and Virion. Fundamental studies about the molecular structure of the spike (S) protein of SARS-CoV-2 using experimental and simulation methods are crucial to the understanding of the virus transmission mechanism in the lung and could contribute to corresponding therapeutic development. Cryogenic electron microscopy (cryo-EM)[176−179] has provided precise measurements of the structure of the full-length S protein in its trimeric form and the S protein-ACE2 complex with angstrom resolution. Computer simulations, such as atomistic molecular dynamics (MD),[180−184] have become a crucial approach to complement experimental studies and provide insight into the structural dynamics of the S protein and its interactions with ligands. Atomistic MD simulations compute trajectories and positions of N interacting atoms in a system by numerically solving Newton's equations of motion.[185,186] Simulations can probe molecular structures with atomistic resolutions and sample MD from subnanoseconds to microseconds and elucidate molecular interactions.[180−182,187−194]

It is worth noting that the computational load using atomistic simulations to study a large-sized system in a long process is prohibitively expensive, particularly with an explicit water model.[181,187,189,195] Based on the current computational capabilities, it is highly challenging to simulate the entire SARS-CoV-2 virion using atomistic MD simulations.[181,196] An atomistic model of a virion such as SARS-CoV-2 and influenza with the diameter of 50−200 nm in water involves more than 200 million atoms, which presents a daunting computational load, requiring about 250,000 processing cores on a high-performance computational cluster.[181,182,187] A recent simulation of four glycosylated S proteins anchored into a patch of viral membrane and embedded in an aqueous solvent with 0.15 M NaCl involved 4.1 million atoms.[182] A viral membrane system of a fully glycosylated full-length S protein with palmitoylation can be built using Membrane Builder of the website: CHARMM-GUI.[180] Amaro and co-workers performed atomistic MD simulations,[181] which consisted of ∼1.7 million atoms, to study the structural dynamics of a full-length glycosylated S protein in explicit water. The protein structure with atomistic resolution can be retrieved from the Protein Data Bank, and the glycomic data about glycan sites of the S protein can be found in literature.[197,198] Molecular interactions between biomolecules and water can be described using common force field parameters, such as Chemistry at Harvard Macromolecular Mechanics (CHARMM),[199−201] Assisted Model Building with Energy Refinement (AMBER),[202−204] and Optimized Potentials for Liquid Simulations-All Atom (OPLS-AA).[205,206]

https://dx.doi.org/10.1021/acsnano.0c08484
ACS Nano 2020, 14, 16502−16524

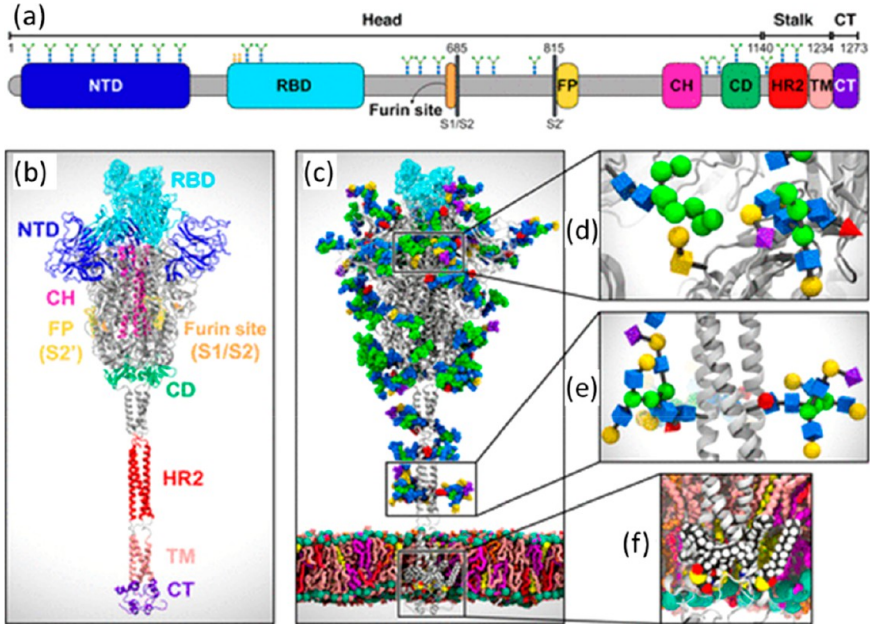

Figure 9. (a) Schematic of the primary structure of the full-length SARS-CoV-2 S protein. It consists of a NTD (16−291), a RBD (330−530), a furin cleavage site (S1/S2), a FP (817−834), a CH (987−1034), a CD (1080−1135), a HR2 (1163−1210), a TM (1214−1234), and a CT (1235−1273). *N*-glycans (blue and green) and *O*-glycan (yellow) are depicted as icons according to their position in the sequence. (b) Atomistic MD simulations of a full-length model of the S protein in the open state consisting of the head, stalk, and CT domains. (c) Atomistic MD simulations of a glycosylated and palmitoylated S protein in the open state embedded in a lipid bilayer, which presents the composition of the endoplasmic reticulum-Golgi intermediate compartment. Protein is shown in gray, with the RBD in the "up" state highlighted with a transparent cyan surface. *N*-/*O*-glycans are shown in van der Waals representation including GlcNAc (blue), mannose (green), fucose (red), galactose (yellow), and sialic acid (purple). Lipids (licorice presentation) contain POPC (pink), POPE (purple), POPI (orange), POPS (red), and cholesterol (yellow). Phosphorus atoms of the lipid heads are colored in green, and cholesterol's O3 atoms are shown in yellow. (d) Magnified view of the S protein head glycosylation. Glycans are presented with the symbol nomenclature for glycans. (e) Magnified view of the S protein stalk glycosylation. (f) Magnified view of the S protein S palmitoylation within CT. Adapted with permission from ref 181. Copyright 2020 American Chemical Society.

To achieve higher efficiency, an alternative method is to use coarse-grained (CG) models instead of full-atom models in MD.[207] In CGMD simulations, the resolution representation is reduced, where a number of atoms are simplified as a CG bead and the intramolecular interaction functions are simplified.[207,208] The general MARTINI force field[209] can be used for CG simulations of proteins and lipids. More precise atomistic or CG models of SARS-CoV-2 and their associated force field parameters, particularly regarding glycans, are still under development, and related information is available in literature[196,210,211] and the open database GitHub.

SARS-CoV-2 and Its S Protein. The SARS-CoV-2 genome encodes approximately 25 proteins, including the S protein, which interacts with human ACE2 receptor in the initial stage of infection, two proteases, which cleave viral and human proteins, the RNA polymerase for synthesizing viral RNA, and the RNA-cleaving endoribonuclease (Figure 8a).[212] The 23 nm long S protein grows on the virus surface as an outward-facing molecular "spike", which is responsible for human infection (Figure 8b).[176,178,179,181,212] The S protein, as a class I fusion trimeric protein, has a single polypeptide chain, which can be divided into three topological domains: the head, stalk, and cytoplasmic tail (CT).[182] Cryo-EM experiments and atomistic MD simulation showed that each stalk has three flexible hinge structures, named the hip, knee, and ankle, that link the S protein to the viral membrane (Figure 8c).[182] The hinges provide the heavily glycosylated head with pronounced orientational flexibility, which is critical for the SARS-CoV-2 S protein to scan and interact with the host cell membranes.[182]

Each monomer of the S protein is composed of two subunits (S1 and S2), including a total of about 22 N-glycosylation sites, in three different domains (head, stalk, and CT) (Figure 9a).[181,198] The S1 subunit contains the N-terminal domain (NTD) and the receptor binding domains (RBD) that interact with ACE2, and the S2 subunit includes the fusion peptide (FP), central helix (CH), connecting domain (CD), heptad repeat 2 (HR2), and transmembrane (TM) domains.[181] The S2 subunit is responsible for membrane fusion, which is key to viral infection.[176,178,179,181] The viral infection process is triggered when the RBD in the S1 subunit of the S protein binds to the peptidase domain (PD) of ACE2, resulting in subsequent exposure and cleavage of the S2 subunit by host proteases.[176,178,179,213] Compared to SARS-CoV, the SARS-CoV-2 S protein has a furin cleavage site between S1 and S2 subunits (S1/S2) (Figure 9a,b).[181] The S1/S2 site can be cleaved by serine proteases, including trypsin, cathepsins, elastase, the host type 2 transmembrane serine protease, and plasmin, facilitating virus entry into epithelial cells.[133,181] Another proteolytic cleavage is found at site S2 that releases the FP, which penetrates the host cell membrane for fusion.[181]

Experimental characterizations[197] showed that the head and stalk domains are extensively covered with glycans (Figure 9c−f). Viral glycosylation plays a wide range of roles in viral pathobiology, such as mediating protein folding and stability and shaping viral tropism and immune recognition.[197] Experimental studies using site-specific mass spectrometric approaches revealed site-specific glycan signatures characteristic of a natively folded trimeric spike.[197] For S proteins, no mannose clusters are

https://dx.doi.org/10.1021/acsnano.0c08484
ACS Nano 2020, 14, 16502−16524

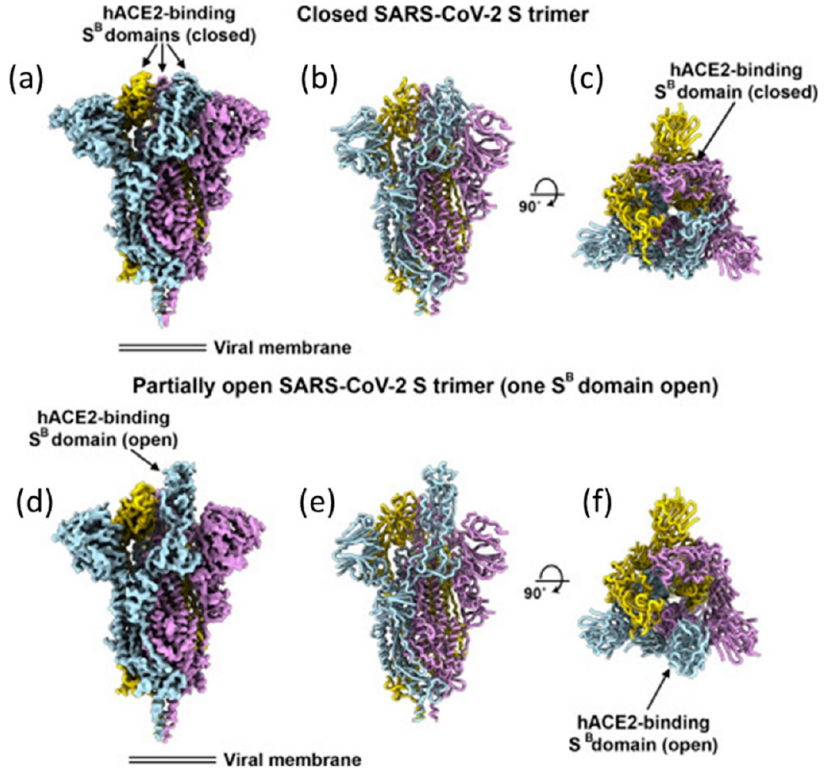

Figure 10. Atomistic conformation of the SARS-CoV-2 S glycoprotein. (a) Closed SARS-CoV-2 S trimer (PDB: 6VXX). (b, c) Two orthogonal views from the side (b) and top (c) of the closed SARS-CoV-2 S trimer. (d) Partially open SARS-CoV-2 S trimer (one S^B domain is open) (PDB: 6VYB). (e, f) Two orthogonal views from the side (e) and top (f) of the open SARS-CoV-2 S trimer. Glycans are omitted for clarity. Adapted with permission from ref 178. Copyright 2020 Elsevier.

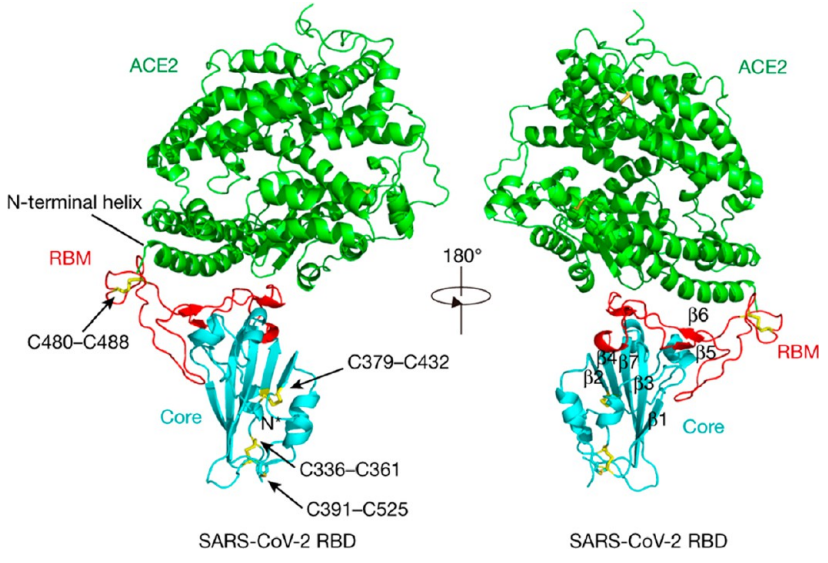

Figure 11. Structure of the SARS-CoV-2 RBD-ACE2 complex. The ACE2 is shown in green, the SARS-CoV-2 RBD core in cyan, and the RBM in red. Disulfide bonds in the SARS-CoV-2 RBD are presented as sticks and also indicated by arrows. The N-terminal helix of the ACE2, which is responsible for binding, is labeled. Adapted with permission from ref 218. Copyright 2020 Springer Nature.

detected compared with LASV GPC and HIV-1 Env. It is worth noting that a recent study using atomistic MD simulations and experiments[181] has shown that besides its functionality of shielding the S protein from antibodies, N-glycans at positions N165 and N234 can modulate the conformational dynamics of the spike's RBD and further enhance the RBD-ACE2 binding.

SARS-CoV-2 is more contagious than other coronaviruses such as SARS-CoV, most likely due to the stronger binding affinity of its S protein, compared with that of SARS-CoV, to ACE2 receptors, even though SARS-CoV-2 shares ~80% sequence identity of the SARS-CoV genome.[176] Composed of three RBDs, which can take different conformations (closed or open) (Figure 10), the S protein head plays a key role in binding receptors.[178,182,214,215] Cryo-EM measurements showed that in the closed conformation, the RBDs are shielded by the N-terminal domains (Figure 10a–c), whereas in the open

https://dx.doi.org/10.1021/acsnano.0c08484
ACS Nano 2020, 14, 16502–16524

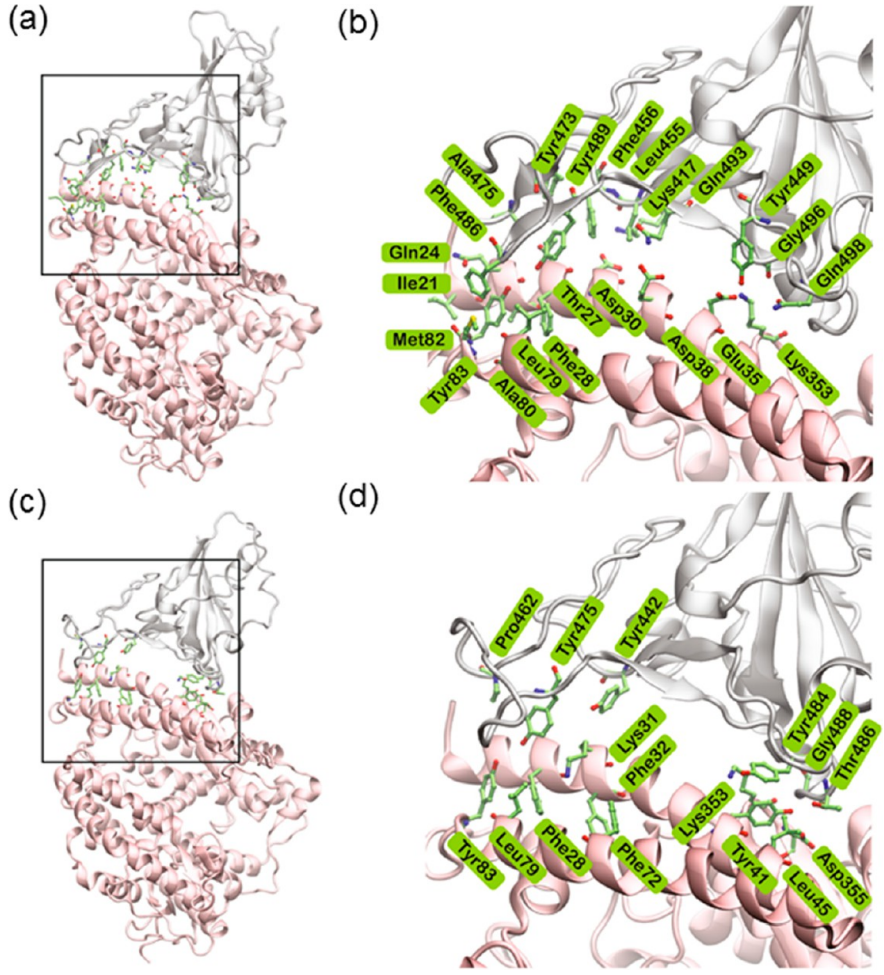

Figure 12. Structural comparisons between (a) SARS-CoV-2 (PDB ID: 6M0J) and (c) SARS-CoV (PDB ID: 2AJF) S protein RBD (gray) bound to an ACE2 receptor (pink). (b, d) Interacting residues in green stick representation, in the magnified regions shown in (a) and (c), respectively. Adapted with permission under a Creative Commons CC BY License from ref 183. Copyright 2020 Springer Nature.

conformation, one RBD is exposed upward in a receptor-accessible conformation (Figure 10d–f).[176,178,182] Atomistic MD simulations indicated that an increased number of interdomain salt bridges in the closed state more likely reduces RBD's mobility compared to in the open state.[216] Free energy landscape analysis also suggested that the salt bridge network is critical to the transition between closed and open states.[216] Moreover, recent studies showed that conformational changes from the open to the closed state can be manipulated by the removal of N-glycans at sites N165 and N234 of the S protein.[181]

Interactions between SARS-CoV-2 S Protein and the ACE2 Receptor. SARS-CoV-2 enters host cells, such as type II alveolar epithelial cells, by binding its S protein with ACE2 receptors expressed on the surface of the host cells.[176,217] Experimental studies reported that the ectodomain of the S protein binds to the ACE2 PD with a dissociation constant (K_d) of ~15 nM, which demonstrates a higher binding affinity compared to SARS-CoV.[176] The SARS-CoV-2 RBD consists of twisted five-stranded antiparallel β sheets (β1–7), short connecting helices, and loops that form the core (Figure 11).[218] There are nine cysteine residues in the RBD and eight of them form four pairs of disulfide bonds. The β sheet structure is stabilized by three cysteine pairs (Cys336-Cys361, Cys379-Cys432, and Cys391-Cys525) in the core. The ACE2 is a dimer accommodating the RBD in its peptidase domain. Two lobes of the N-terminal peptidase domain of the ACE2 form the peptide substrate binding site between them. A concave outer surface in the receptor-binding motif (RBM) of the SARS-CoV-2 RBD binds to the N-terminal helix of the ACE2 (Figure 11).[218] The ACE2 PD uses the α1-helix as its primary contact to bind RBD, though the ACE2 α2-helix and the linker of the β3- and β4-sheets also help.[179,218]

Studies of interactions among the amino acids at the interface between the SARS-CoV-2 RBD and the ACE2 PD are crucial to the understanding of virus transmission in the lung and thus for inhibitor design. Atomistic MD simulations suggested that the S protein-ACE2 binding is governed by hydrogen bonding, electrostatic interactions, and hydrophobic interactions.[181,183] There are three unique stable hydrogen bonds between SARS-CoV-2 S protein's residues (Tyr449, Gln493, and Gln498) and ACE2 residues (Asp38, Glu35, and Lys353) at the binding interface (Figure 12a,b), compared to SARS-CoV (Figure 12c,d).[183] Residues (Tyr473, Ala475, and Phe486) of SARS-CoV-2 form hydrophobic interactions with ACE2 residues (Figure 12b).[183] In the middle region of the binding interface, besides hydrophobic interactions between Phe456 and Tyr489 of the S protein and Thr27 of ACE2, there is a strong salt bridge between Lys417 of the S protein and Asp30 of ACE2 (Figure 12b), which increases the S protein-ACE2 electrostatic

https://dx.doi.org/10.1021/acsnano.0c08484
ACS Nano 2020, 14, 16502–16524

interactions and therefore further stabilizes the complex structure.[183]

Both the S protein and ACE2 contain disulfide bonds between cysteine residues. Atomistic MD simulation and free energy computation showed that the binding affinity between the S protein and ACE2 becomes weaker when the disulfides of ACE2 are reduced to sulfydryl groups.[219] However, the S protein-ACE2 binding is insensitive to the reduction of disulfide in the S protein's RBD.[219] Atomistic MD simulations showed that the absolute value of binding free energy between SARS-CoV-2 S protein and human ACE2 is 9.5 kcal/mol greater than that with pangolin ACE2. Human ACE2 is among the most polymorphous gene and has 317 missense single-nucleotide variations (SNVs).[220] Different SNVs exhibit different binding affinity with the S proteins.[220] Han and Kral performed atomistic MD simulations to study the binding mechanism of peptide inhibitors of SARS-CoV-2.[221] Their study demonstrated that the pronounced structural stability of α-helical peptide bundle extracted from the ACE2 PD is critical to their binding specificity to the RBD of SARS-CoV-2.[221] Their work also suggested that nanoparticle carriers with many such peptides can provide multivalent binding and full coverage to SARS-CoV-2 receptors.[221]

Recent CGMD simulations elucidated that the unique polybasic cleavage site of $R_{682}RAR_{685}$ (*i.e.*, S1/S2 on Figure 9a) of SARS-CoV-2 S protein can enhance the binding affinity of the S protein's RBD with ACE2 *via* electrostatic interactions and hydration bonding, although they are about 10 nm away from the RBD (Figure 13).[222] The simulations further demonstrated

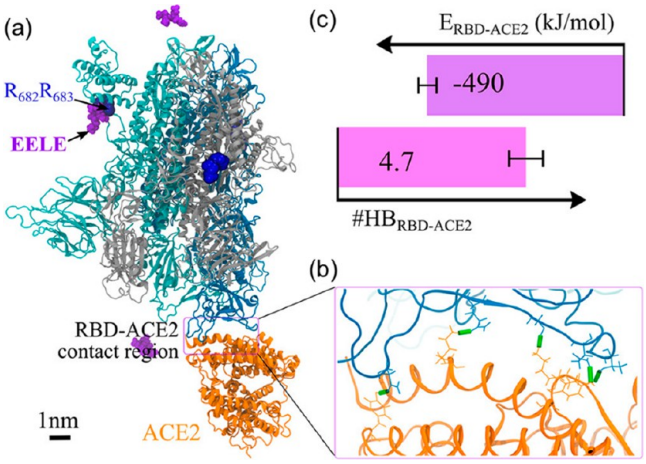

Figure 13. Binding of tetrapeptide GluGluLeuGlu (EELE) weakens the RBD-ACE2 binding affinity. (a) MD simulation of a spike-ACE2 complex with the binding of EELE (violet). (b) Magnified RBD-ACE2 contact region, where the RBD-ACE2 intermolecular hydrogen bonds are highlighted *via* green sticks. (c) RBD-ACE2 interaction potential energy and the number of hydrogen bonds. Adapted with permission from ref 222. Copyright 2020 American Chemical Society.

that the binding of a negatively charged tetrapeptide (GluGluLeuGlu) to one of the three polybasic cleavage sites, which are positively charged, reduces the RBD-ACE2 binding strength by 34%.[222] Consistent with these findings, experiments showed that the mutation of the $T_{678}NSPRRAR_{685}$ residues in S protein to a variant of T_{678}-IL-R_{685} lowered the SARS-CoV-2 transduction efficiency in human ACE2-expressing baby hamster kidney cells.[178]

To predict immunogenic regions, Colombo and co-workers performed an energetic coupling analysis on a solvated fully glycosylated S protein using atomistic MD simulation trajectories.[184] Their structure-based computational approach showed antibody recognition sites (epitopes) can be correlated to localized regions, which exhibit only low-intensity energetic coupling with the rest of the structure and display large functional conformational transitions.[184] The three most antigenic regions identified were: the upward part of RBDs, including the N-terminal domain, and the central/C-terminal part of the S1A domain (Figure 14a,b), which corresponds to

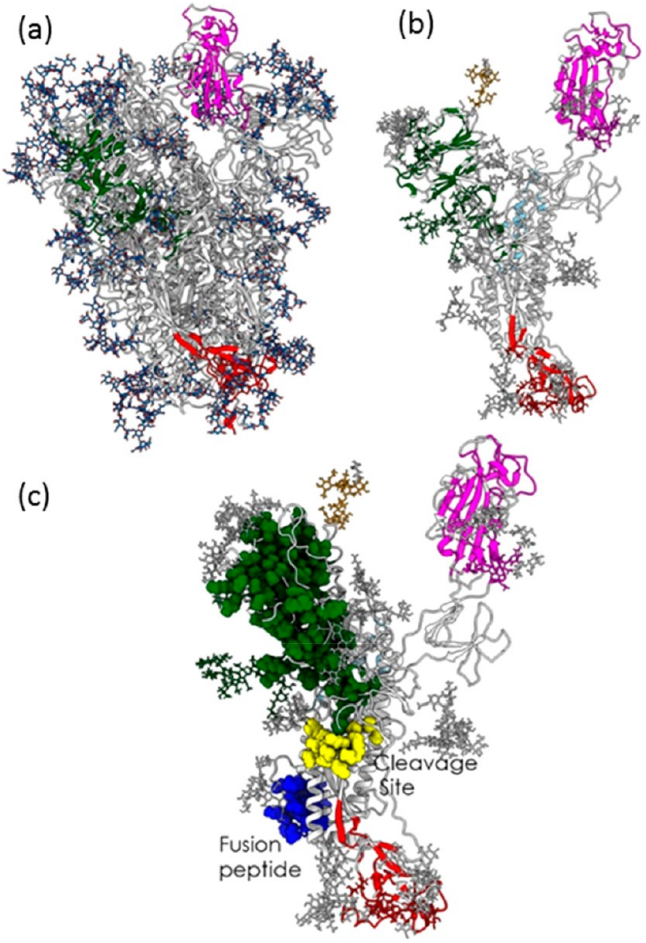

Figure 14. MD simulations of (a) the SARS-CoV-2 fully glycosylated S protein trimer. The coating oligosaccharides are shown in dark blue. (b) The immunogenic domains analyzed by decomposition. The antigenic part in the N-terminal domain is shown in dark green, the upper part in the RBD in magenta, and the part in the C-terminal domain in dark red. Oligosaccharides that have strong energetic coupling to the protein are colored in white. (c) The immunogenic domains, cleavage site (yellow), and fusion peptide (blue). Adapted with permission from ref 184. Copyright 2020 American Chemical Society.

the binding region of the monoclonal antibody CR3022, the binding region of the new antibody 484, and the antigen-binding fragments of COV57, respectively.[184] From the tertiary structure, the boundary of the N-terminal region locates close to the furin-targeted motif RRAR (Figure 14c), which is critical to preactivation of the S protein through proteolysis.[184] The β-sheet at the initial boundary of the C-terminal domain in the S2 subunit is near the fusion peptide (Figure 14c).[184] It was also

https://dx.doi.org/10.1021/acsnano.0c08484
ACS Nano 2020, 14, 16502−16524

found that glycans with stronger energetic coupling protect underlying peptidic epitopes, such as N165-linked oligosaccharide.[184] In contrast, glycans with weaker energetic coupling can enhance antibody recognition, for example, an oligosaccharide fragment bound to N234,[184] an observation which was also reported in the work of Amaro and co-workers.[181]

Future Directions in Molecular Dynamics Simulations of Virus−Receptor Interactions. A comprehensive understanding of the structural dynamics of SARS-CoV-2 S protein and virion, along with their interactions with the ACE2 receptor at the atomistic and molecular levels, is critical to the development of vaccines and therapeutics. Atomistic MD simulations, which are based on the well-calibrated force field parameters and experimental measurements of protein structure, have been extensively employed to offer insights into the SARS-CoV-2 biomolecules with atomistic resolution. However, it presents a major challenge to perform atomistic MD simulations to model the entire virion in an explicit water environment involving hundreds of millions of atoms with a prolonged time scale, due to the heavy computational load. Most recent simulations only focused on the atomistic modeling of a fully glycosylated S protein without and with the viral membrane instead of an entire virion. More efficient CGMD simulations, which can present molecular structural changes, are still under development, and reliable force field parameters are not yet available.

Complementary to experimental measurements, atomistic MD simulations have revealed structures of the S protein, including its subunits, RBDs, plausible active sites, and location of surface glycans, structural stability, and its interaction with receptors. Simulations showed that a SARS-CoV-2 S protein displays an extremely high rotational structural flexibility at the connection regions between the headgroup and cell membranes, which helps the virus locate and interact with the ACE2 acceptor of human cells. Analysis of the binding free energy showed that the binding affinity between SARS-CoV-2 and the ACE2 receptor is higher than that with SARS-CoV due to its domain structural stability, strong hydrophobic and electrostatic interactions, and unique hydrogen bonds. Extraordinary efforts have been exerted to predict active sites of the S protein for the purpose of controlling the viral binding. Glycans covering the cell surface were found not only to protect the virus from antibody recognition but also to contribute to the viral binding with ACE2. It is noteworthy that several critical issues remain unknown for an in-depth understanding of the virus transmission *via* aerosols. It is still unknown how the S protein interacts with aerosol surfaces and biomembranes at the atomistic and molecular levels, which is a critical issue that determines the affinity and transmission of the virus *via* aerosols. The effect of water content on the S protein structure on the aerosol surfaces and their correlation with virus survival time need further investigation. MD simulations hold promise for all of these investigations.

CONCLUDING REMARKS

Engineering, physical, and chemical sciences have much to contribute toward the global fight against the COVID-19 pandemic. In particular, aerosols are strongly suspected to play a significant role in the rapid spread of the disease. Key steps in the hypothesized airborne transmission pathway, from the initial aerosol ejection by a cough or exhalation to deposition of the virus-laden aerosols in the lung and to the binding of the S protein of SARS-CoV-2 to the ACE2 receptor on the surface of a host cell, are largely governed by physicochemical mechanisms, that is, the exchange of mass, energy, and momentum between virions, aerosol particles, and the surrounding environment. Viewing COVID-19 transmission through the lens of bioaerosol mechanics may lead to the development of mitigation approaches, such as rational ventilation protocols, antiviral materials and coatings, and even new therapeutic interventions, such as the surfactant therapy to alleviate COVID-19-induced ARDS symptoms. Although we have no expectation of a "magic bullet" against COVID-19, widespread adoption of physically and chemically motivated and justified mitigation strategies would effectively reduce the virus reproduction rate R_0, giving relief to stressed medical systems and healthcare providers and saving hundreds of thousands of lives. Indeed, after the first few months of the pandemic, most governments and individuals have come to understand and accept the effectiveness of simple face coverings, which may greatly reduce the chance of airborne transmission.

The pandemic has also revealed gaps in our understanding about particulate matter and bioaerosol mechanics. For instance, dispersal of infectious virus-laden aerosols in air and their deposition onto general surfaces and various regions of the lung are multiscale and multiphysical processes. Accordingly, it is challenging to identify and select all relevant contributing physicochemical processes and resolve them under the framework of one unified computational or analytical model. On the one hand, the CFD approach has demonstrated success in modeling aerosol transmission by air flow in built environments. On the other hand, MD simulations have demonstrated particular impacts on revealing specific virus−receptor interactions at the atomistic and molecular scales. Effective multiscale interfacing and exchanging parameters between the micro-to-macroscale CFD modeling and the atomistic-to-molecular scale MD simulations, however, have proven to be technically challenging. Several key fundamental questions remain open. For example, correlations between the virus viability and the S protein denaturation on the aerosol surface are still unknown. The effects of water content and physicochemical properties of the aerosols on the S protein structural dynamics and virion packing remain largely undefined. A comprehensive understanding of the complete pathway for the airborne transmission of COVID-19 is yet to be established.

Although plausible, direct clinical evidence for lung infection by virus-laden aerosols is still lacking. It is also unknown whether the virus-laden aerosols, especially those within the most breathable size range between 0.5 and 5 μm, can carry SARS-CoV-2 deep to the terminal alveoli. However, if this transmission pathway does exist, it would bypass the mucociliary clearance and incubation period of the virus in the upper airways and thus cause direct detrimental effects on the alveolar regions of the lung, which would greatly change the progression of the disease. This could also in part explain the widely differential symptoms and clinical outcomes for COVID-19 patients even in a seemingly homogeneous population. In the alveolar region, interactions with the endogenous PS would determine the subsequent macrophage clearance of the virus-laden aerosols and interactions between the virus and ACE2 receptors expressed on the surface of alveolar type II cells. Synergetic effects between direct surfactant inhibition and reduced surfactant metabolism would worsen lung homeostasis and cause alveolar collapse and instability, thus, in the most severe cases, leading to the ARDS symptoms of pulmonary edema and alveolar flooding. Hence, there is a strong rationale for surfactant

https://dx.doi.org/10.1021/acsnano.0c08484
ACS Nano 2020, 14, 16502−16524

replacement as a plausible supportive therapy to treat COVID-19 patients. We hope this review provides useful multidisciplinary knowledge that helps understanding and ultimately contributes to curbing the airborne transmission of COVID-19.

AUTHOR INFORMATION

Corresponding Authors

Yi Y. Zuo − *Department of Mechanical Engineering, University of Hawaii at Manoa, Honolulu, Hawaii 96822, United States; Department of Pediatrics, John A. Burns School of Medicine, University of Hawaii, Honolulu, Hawaii 96826, United States;* orcid.org/0000-0002-3992-3238; Email: yzuo@hawaii.edu

William E. Uspal − *Department of Mechanical Engineering, University of Hawaii at Manoa, Honolulu, Hawaii 96822, United States;* orcid.org/0000-0003-3335-5900; Email: uspal@hawaii.edu

Tao Wei − *Chemical Engineering Department, Howard University, Washington, DC 20059, United States;* orcid.org/0000-0001-6888-1658; Email: tao.wei@howard.edu

Complete contact information is available at: https://pubs.acs.org/10.1021/acsnano.0c08484

Notes

The authors declare no competing financial interest.

ACKNOWLEDGMENTS

We thank Drs. Fred Possmayer and Neil Uspal for valuable discussion about our paper. This research was supported by the National Science Foundation (NSF) grant numbers CBET-1604119 and CBET-2011317 to Y.Y.Z., the American Chemical Society (ACS) Petroleum Research Fund grant number 60809-DNI9 to W.E.U., and NSF grant numbers CBET-1831559 and CBET-1943999 to T.W.

VOCABULARY

COVID-19, coronavirus disease 2019, is the disease that is causing a global pandemic; **SARS-CoV-2**, severe acute respiratory syndrome coronavirus 2, is the virus that causes COVID-19; **ACE2**, angiotensin converting enzyme 2, is the human receptor responsible for SARS-CoV-2 entry into cells; **RBD**, receptor binding domain, is a key part of the viral spike protein that allows it to dock to the receptor for cell entry; **PS**, pulmonary surfactant, is a lipid−protein complex that is synthesized by the alveolar type II epithelial cells and is responsible for innate immunity and surface tension reduction in the lung; **MD**, molecular dynamics, is a computer simulation method for studying the physical movements and interactions between atoms and molecules; **CFD**, computational fluid dynamics, is a branch of fluid mechanics concerned with numerical methods for the solution of physical problems involving fluid flow

REFERENCES

(1) *Coronavirus Disease (COVID-19) Pandemic*. https://www.who.int/emergencies/diseases/novel-coronavirus-2019 (accessed 2020-11-15).

(2) Millett, G. A.; Jones, A. T.; Benkeser, D.; Baral, S.; Mercer, L.; Beyrer, C.; Honermann, B.; Lankiewicz, E.; Mena, L.; Crowley, J. S.; Sherwood, J.; Sullivan, P. Assessing Differential Impacts of COVID-19 on Black Communities. *Annals of Epidemiology* **2020**, *47*, 37−44.

(3) Haynes, N.; Cooper, L. A.; Albert, M. A. At the Heart of the Matter: Unmasking and Addressing COVID-19's Toll on Diverse Populations. *Circulation* **2020**, *142* (2), 105−107.

(4) O'Dowd, A. Guidance Needed for Singlehanded GPs to Deal with COVID-19 Pandemic. *BMJ.* **2020**, *368*, m1261.

(5) Yancy, C. W. COVID-19 and African Americans. *JAMA* **2020**, *323* (19), 1891−1892.

(6) Kaholokula, J. K.; Samoa, R. A.; Miyamoto, R. E. S.; Palafox, N.; Daniels, S.-A. COVID-19 Special Column: COVID-19 Hits Native Hawaiian and Pacific Islander Communities the Hardest. *Hawaii J Health Soc. Welf.* **2020**, *79* (5), 143−146.

(7) Webb Hooper, M.; Nápoles, A. M.; Pérez-Stable, E. J. COVID-19 and Racial/Ethnic Disparities. *JAMA* **2020**, *323* (24), 2466−2467.

(8) Belanger, M. J.; Hill, M. A.; Angelidi, A. M.; Dalamaga, M.; Sowers, J. R.; Mantzoros, C. S. COVID-19 and Disparities in Nutrition and Obesity. *N. Engl. J. Med.* **2020**, *383* (11), No. e69.

(9) Li, Q.; Guan, X.; Wu, P.; Wang, X.; Zhou, L.; Tong, Y.; Ren, R.; Leung, K. S. M.; Lau, E. H. Y.; Wong, J. Y.; Xing, X.; Xiang, N.; Wu, Y.; Li, C.; Chen, Q.; Li, D.; Liu, T.; Zhao, J.; Liu, M.; Tu, W.; et al. Early Transmission Dynamics in Wuhan, China, of Novel Coronavirus−Infected Pneumonia. *N. Engl. J. Med.* **2020**, *382* (13), 1199−1207.

(10) *Modes of Transmission of Virus Causing COVID-19: Implications for IPC Precaution Recommendations*. https://www.who.int/news-room/commentaries/detail/modes-of-transmission-of-virus-causing-covid-19-implications-for-ipc-precaution-recommendations (accessed 2020-03-29).

(11) Goldman, E. Exaggerated Risk of Transmission of COVID-19 by Fomites. *Lancet Infect. Dis.* **2020**, *20* (8), 892−893.

(12) Mondelli, M. U.; Colaneri, M.; Seminari, E. M.; Baldanti, F.; Bruno, R. Low risk of SARS-CoV-2 Transmission by Fomites in Real-Life Conditions. *Lancet Infect. Dis.* **2020**, DOI: 10.1016/S1473-3099(20)30678-2.

(13) *How COVID-19 Spreads*. https://www.cdc.gov/coronavirus/2019-ncov/prevent-getting-sick/how-covid-spreads.html (accessed 2020-10-28).

(14) *Report of the WHO-China Joint Mission on Coronavirus Disease 2019 (COVID-19)*. https://www.who.int/docs/default-source/coronaviruse/who-china-joint-mission-on-covid-19-final-report.pdf) (accessed 2020-02-28).

(15) Tellier, R.; Li, Y.; Cowling, B. J.; Tang, J. W. Recognition of Aerosol Transmission of Infectious Agents: A Commentary. *BMC Infect. Dis.* **2019**, *19* (1), 101.

(16) Poulain, S.; Bourouiba, L. Disease Transmission *via* Drops and Bubbles. *Phys. Today* **2019**, *72* (5), 70−71.

(17) Morawska, L.; Tang, J. W.; Bahnfleth, W.; Bluyssen, P. M.; Boerstra, A.; Buonanno, G.; Cao, J.; Dancer, S.; Floto, A.; Franchimon, F.; Haworth, C.; Hogeling, J.; Isaxon, C.; Jimenez, J. L.; Kurnitski, J.; Li, Y.; Loomans, M.; Marks, G.; Marr, L. C.; Mazzarella, L.; et al. How can Airborne Transmission of COVID-19 Indoors be Minimised? *Environ. Int.* **2020**, *142*, 105832.

(18) Buonanno, G.; Stabile, L.; Morawska, L. Estimation of Airborne Viral Emission: Quanta Emission Rate of SARS-CoV-2 for Infection Risk Assessment. *Environ. Int.* **2020**, *141*, 105794.

(19) Dancer, S. J.; Tang, J. W.; Marr, L. C.; Miller, S.; Morawska, L.; Jimenez, J. L. Putting a Balance on the Aerosolization Debate around SARS-CoV-2. *Journal of Hospital Infection* **2020**, *105* (3), 569−570.

(20) Morawska, L.; Cao, J. Airborne Transmission of SARS-CoV-2: The World Should Face the Reality. *Environ. Int.* **2020**, *139*, 105730.

(21) Kumar, P.; Morawska, L. Could Fighting Airborne Transmission Be the Next Line of Defence Against COVID-19 Spread? *City and Environment Interactions* **2019**, *4*, 100033.

(22) Prather, K. A.; Wang, C. C.; Schooley, R. T. Reducing Transmission of SARS-CoV-2. *Science* **2020**, *368* (6498), 1422−1424.

(23) Morawska, L.; Milton, D. K. It is Time to Address Airborne Transmission of COVID-19. *Clin. Infect. Dis.* **2020**, *6*, ciaa939.

(24) Fennelly, K. P. Particle Sizes of Infectious Aerosols: Implications for Infection Control. *Lancet Respir. Med.* **2020**, *8* (9), 914−924.

(25) Bourouiba, L. Turbulent Gas Clouds and Respiratory Pathogen Emissions: Potential Implications for Reducing Transmission of COVID-19. *JAMA* **2020**, *323* (18), 1837−1838.
(26) Scheuch, G. Breathing Is Enough: For the Spread of Influenza Virus and SARS-CoV-2 by Breathing Only. *J. Aerosol Med. Pulm. Drug Delivery* **2020**, *33* (4), 230−234.
(27) Ma, J.; Qi, X.; Chen, H.; Li, X.; Zhang, Z.; Wang, H.; Sun, L.; Zhang, L.; Guo, J.; Morawska, L.; Grinshpun, S. A.; Biswas, P.; Flagan, R. C.; Yao, M. Coronavirus Disease 2019 Patients in Earlier Stages Exhaled Millions of Severe Acute Respiratory Syndrome Coronavirus 2 per Hour. *Clin. Infect. Dis.* **2020**, ciaa1283.
(28) Bake, B.; Larsson, P.; Ljungkvist, G.; Ljungström, E.; Olin, A. C. Exhaled Particles and Small Airways. *Respir. Res.* **2019**, *20* (1), 8.
(29) Xie, X.; Li, Y.; Chwang, A. T.; Ho, P. L.; Seto, W. H. How Far Droplets can Move in Indoor Environments–Revisiting the Wells Evaporation-Falling Curve. *Indoor Air* **2007**, *17* (3), 211−25.
(30) Liang, D.; Shi, L.; Zhao, J.; Liu, P.; Schwartz, J.; Gao, S.; Sarnat, J. A.; Liu, Y.; Ebelt, S. T.; Scovronick, N. C.; Chang, H. Urban Air Pollution May Enhance COVID-19 Case-Fatality and Mortality Rates in the United States. *Innovation* **2020**, *1*, 100047.
(31) Conticini, E.; Frediani, B.; Caro, D. Can Atmospheric Pollution Be Considered a Co-Factor in Extremely High Level of SARS-CoV-2 Lethality in Northern Italy? *Environ. Pollut.* **2020**, *261*, 114465.
(32) Wu, X.; Nethery, R. C.; Sabath, B. M.; Braun, D.; Dominici, F. Air Pollution and COVID-19 Mortality in the United States: Strengths and Limitations of an Ecological Regression Analysis. *Sci. Adv.* **2020**, *6* (45), No. eabd4049.
(33) Moriyama, M.; Hugentobler, W. J.; Iwasaki, A. Seasonality of Respiratory Viral Infections. *Annu. Rev. Virol.* **2020**, *7* (1), 83−101.
(34) Luo, W.; Majumder, M. S.; Liu, D.; Poirier, C.; Mandl, K. D.; Lipsitch, M.; Santillana, M. The Role of Absolute Humidity on Transmission Rates of the COVID-19 Outbreak. *medRxiv*, February 17, 2020, ver. 1.https://www.medrxiv.org/content/10.1101/2020.02.12.20022467v1 (accessed 2020-02-17).
(35) Javelle, E. Electronic Cigarette and Vaping Should Be Discouraged During the New Coronavirus SARS-CoV-2 Pandemic. *Arch. Toxicol.* **2020**, *94* (6), 2261−2262.
(36) McAlinden, K. D.; Eapen, M. S.; Lu, W.; Chia, C.; Haug, G.; Sohal, S. S. COVID-19 and Vaping: Risk for Increased Susceptibility to SARS-CoV-2 Infection? *Eur. Respir. J.* **2020**, *56*, 2001645.
(37) *Consensus Document on the Epidemiology of Severe Acute Respiratory Syndrome (SARS)*. https://apps.who.int/iris/handle/10665/70863 (accessed 2020-11-15).
(38) Gormley, M.; Aspray, T. J.; Kelly, D. A. COVID-19: Mitigating Transmission *via* Wastewater Plumbing Systems. *Lancet. Global health* **2020**, *8* (5), No. e643.
(39) Miller, S. L.; Nazaroff, W. W.; Jimenez, J. L.; Boerstra, A.; Buonanno, G.; Dancer, S. J.; Kurnitski, J.; Marr, L. C.; Morawska, L.; Noakes, C. Transmission of SARS-CoV-2 by Inhalation of Respiratory Aerosol in the Skagit Valley Chorale Superspreading Event. *Indoor Air* **2020**, *00*, 1−10.
(40) Lu, J.; Gu, J.; Li, K.; Xu, C.; Su, W.; Lai, Z.; Zhou, D.; Yu, C.; Xu, B.; Yang, Z. COVID-19 Outbreak Associated with Air Conditioning in Restaurant, Guangzhou, China, 2020. *Emerging Infect. Dis.* **2020**, *26* (7), 1628−1631.
(41) Guo, Z.-D.; Wang, Z.-Y.; Zhang, S.-F.; Li, X.; Li, L.; Li, C.; Cui, Y.; Fu, R.-B.; Dong, Y.-Z.; Chi, X.-Y.; Zhang, M.-Y.; Liu, K.; Cao, C.; Liu, B.; Zhang, K.; Gao, Y.-W.; Lu, B.; Chen, W. Aerosol and Surface Distribution of Severe Acute Respiratory Syndrome Coronavirus 2 in Hospital Wards, Wuhan, China, 2020. *Emerging Infect. Dis.* **2020**, *26* (7), 1583−1591.
(42) Liu, Y.; Ning, Z.; Chen, Y.; Guo, M.; Liu, Y.; Gali, N. K.; Sun, L.; Duan, Y.; Cai, J.; Westerdahl, D.; Liu, X.; Xu, K.; Ho, K.-f.; Kan, H.; Fu, Q.; Lan, K. Aerodynamic Analysis of SARS-CoV-2 in Two Wuhan Hospitals. *Nature* **2020**, *582* (7813), 557−560.
(43) van Doremalen, N.; Bushmaker, T.; Morris, D. H.; Holbrook, M. G.; Gamble, A.; Williamson, B. N.; Tamin, A.; Harcourt, J. L.; Thornburg, N. J.; Gerber, S. I.; Lloyd-Smith, J. O.; de Wit, E.; Munster, V. J. Aerosol and Surface Stability of SARS-CoV-2 as Compared with SARS-CoV-1. *N. Engl. J. Med.* **2020**, *382* (16), 1564−1567.
(44) Zhu, N.; Zhang, D.; Wang, W.; Li, X.; Yang, B.; Song, J.; Zhao, X.; Huang, B.; Shi, W.; Lu, R.; Niu, P.; Zhan, F.; Ma, X.; Wang, D.; Xu, W.; Wu, G.; Gao, G. F.; Tan, W. A Novel Coronavirus from Patients with Pneumonia in China, 2019. *N. Engl. J. Med.* **2020**, *382* (8), 727−733.
(45) Bar-On, Y. M.; Flamholz, A.; Phillips, R.; Milo, R. SARS-CoV-2 (COVID-19) by the Numbers. *eLife* **2020**, *9*, No. e57309.
(46) Zuo, Z.; Kuehn, T. H.; Bekele, A. Z.; Mor, S. K.; Verma, H.; Goyal, S. M.; Raynor, P. C.; Pui, D. Y. H. Survival of Airborne MS2 Bacteriophage Generated from Human Saliva, Artificial Saliva, and Cell Culture Medium. *Appl. Environ. Microbiol.* **2014**, *80* (9), 2796−2803.
(47) Couch, R. B.; Knight, V.; Douglas, R. G., Jr.; Black, S. H.; Hamory, B. H. The Minimal Infectious Dose of Adenovirus Type 4; the Case for Natural Transmission by Viral Aerosol. *Trans Am. Clin. Climatol. Assoc.* **1969**, *80*, 205−211.
(48) Poon, W. C. K.; Brown, A. T.; Direito, S. O. L.; Hodgson, D. J. M.; Le Nagard, L.; Lips, A.; MacPhee, C. E.; Marenduzzo, D.; Royer, J. R.; Silva, A. F.; Thijssen, J. H. J.; Titmuss, S. Soft Matter Science and the COVID-19 Pandemic. *Soft Matter* **2020**, *16* (36), 8310−8324.
(49) Morawska, L.; Johnson, G. R.; Ristovski, Z. D.; Hargreaves, M.; Mengersen, K.; Corbett, S.; Chao, C. Y. H.; Li, Y.; Katoshevski, D. Size Distribution and Sites of Origin of Droplets Expelled from the Human Respiratory Tract During Expiratory Activities. *J. Aerosol Sci.* **2009**, *40* (3), 256−269.
(50) Yang, S.; Lee, G. W.M.; Chen, C.-M.; Wu, C.-C.; Yu, K.-P. The Size and Concentration of Droplets Generated by Coughing in Human Subjects. *J. Aerosol Med.* **2007**, *20* (4), 484−494.
(51) Balachandar, S.; Zaleski, S.; Soldati, A.; Ahmadi, G.; Bourouiba, L. Host-to-Host Airborne Transmission as a Multiphase Flow Problem for Science-Based Social Distance Guidelines. *Int. J. Multiphase Flow* **2020**, *132*, 103439.
(52) Netz, R. R. Mechanisms of Airborne Infection *via* Evaporating and Sedimenting Droplets Produced by Speaking. *J. Phys. Chem. B* **2020**, *124* (33), 7093−7101.
(53) Marr, L. C.; Tang, J. W.; Van Mullekom, J.; Lakdawala, S. S. Mechanistic Insights into the Effect of Humidity on Airborne Influenza Virus Survival, Transmission and Incidence. *J. R. Soc. Interface* **2019**, *16* (150), 20180298.
(54) Duguid, H. A.; Stampfer, J. F., Jr. The Evaporation Rates of Small, Freely Falling Water Drops. *J. Atmos. Sci.* **1971**, *28* (7), 1233−1243.
(55) Crespo, A.; LiÑAn, A. Unsteady Effects in Droplet Evaporation and Combustion. *Combust. Sci. Technol.* **1975**, *11* (1−2), 9−18.
(56) Kinzer, G. D.; Gunn, R. The Evaporation, Temperature and Thermal Relaxation-Time of Freely Falling Waterdrops. *J. Meteorol.* **1951**, *8* (2), 71−83.
(57) Sazhin, S. S. Advanced Models of Fuel Droplet Heating and Evaporation. *Prog. Energy Combust. Sci.* **2006**, *32* (2), 162−214.
(58) Lupo, G.; Niazi Ardekani, M.; Brandt, L.; Duwig, C. An Immersed Boundary Method for Flows with Evaporating Droplets. *Int. J. Heat Mass Transfer* **2019**, *143*, 118563.
(59) Schlottke, J.; Weigand, B. Direct Numerical Simulation of Evaporating Droplets. *J. Comput. Phys.* **2008**, *227* (10), 5215−5237.
(60) Newbold, F. R.; Amundson, N. R. A Model for Evaporation of a Multicomponent Droplet. *AIChE J.* **1973**, *19* (1), 22−30.
(61) Michaelides, E. E. Hydrodynamic Force and Heat/Mass Transfer from Particles, Bubbles, and Drops—The Freeman Scholar Lecture. *J. Fluids Eng.* **2003**, *125* (2), 209−238.
(62) Netz, R. R.; Eaton, W. A. Physics of Virus Transmission by Speaking Droplets. *Proc. Natl. Acad. Sci. U. S. A.* **2020**, *117* (41), 25209−25211.
(63) Verreault, D.; Moineau, S.; Duchaine, C. Methods for Sampling of Airborne Viruses. *Microbiol. Mol. Biol. Rev.* **2008**, *72* (3), 413−444.
(64) Duguid, J. P. The Size and the Duration of Air-Carriage of Respiratory Droplets and Droplet-Nuclei. *Epidemiol. Infect.* **1946**, *44* (6), 471−479.
(65) Vejerano, E. P.; Marr, L. C. Physico-Chemical Characteristics of Evaporating Respiratory Fluid Droplets. *J. R. Soc. Interface* **2018**, *15* (139), 20170939.

https://dx.doi.org/10.1021/acsnano.0c08484
ACS Nano 2020, 14, 16502−16524

(66) Fedorenko, A.; Grinberg, M.; Orevi, T.; Kashtan, N. Virus Survival in Evaporated Saliva Microdroplets Deposited on Inanimate Surfaces. *bioRxiv*, June 16, 2020, ver. 1.https://www.biorxiv.org/content/10.1101/2020.06.15.152983v1 (accessed 2020-11-10).
(67) Vonnemann, J.; Sieben, C.; Wolff, C.; Ludwig, K.; Böttcher, C.; Herrmann, A.; Haag, R. Virus Inhibition Induced by Polyvalent Nanoparticles of Different Sizes. *Nanoscale* **2014**, *6* (4), 2353−2360.
(68) Arakelyan, A.; Fitzgerald, W.; Margolis, L.; Grivel, J.-C. Nanoparticle-Based Flow Virometry for the Analysis of Individual Virions. *J. Clin. Invest.* **2013**, *123* (9), 3716−3727.
(69) Leung, W. W.-F.; Sun, Q. Charged PVDF Multilayer Nanofiber Filter in Filtering Simulated Airborne Novel Coronavirus (COVID-19) Using Ambient Nano-Aerosols. *Sep. Purif. Technol.* **2020**, *245*, 116887−116887.
(70) Weissman, D. N.; de Perio, M. A.; Radonovich, L. J., Jr COVID-19 and Risks Posed to Personnel During Endotracheal Intubation. *JAMA* **2020**, *323* (20), 2027−2028.
(71) Barker, J.; Jones, M. V. The Potential Spread of Infection Caused by Aerosol Contamination of Surfaces after Flushing a Domestic Toilet. *J. Appl. Microbiol.* **2005**, *99* (2), 339−347.
(72) Liu, X.; Zhai, Z. Identification of Appropriate CFD Models for Simulating Aerosol Particle and Droplet Indoor Transport. *Indoor Built Environ.* **2007**, *16* (4), 322−330.
(73) Blocken, B. LES over RANS in Building Simulation for Outdoor and Indoor Applications: A Fregone Conclusion? *Building Simulation* **2018**, *11* (5), 821−870.
(74) Buchanan, C. R.; Dunn-Rankin, D. Transport of Surgically Produced Aerosols in an Operating Room. *Am. Ind. Hyg. Assoc. J.* **1998**, *59* (6), 393−402.
(75) Li, Y.; Huang, X.; Yu, I. T. S.; Wong, T. W.; Qian, H. Role of Air Distribution in SARS Transmission during the Largest Nosocomial Outbreak in Hong Kong. *Indoor Air* **2005**, *15* (2), 83−95.
(76) Vilela, R. D.; Motter, A. E. Can Aerosols Be Trapped in Open Flows? *Phys. Rev. Lett.* **2007**, *99* (26), 264101.
(77) Sun, W.; Ji, J. Transport of Droplets Expelled by Coughing in Ventilated Rooms. *Indoor Built Environ.* **2007**, *16* (6), 493−504.
(78) Schmidt, L.; Fouxon, I.; Krug, D.; van Reeuwijk, M.; Holzner, M. Clustering of Particles in Turbulence Due to Phoresis. *Phys. Rev. E: Stat. Phys., Plasmas, Fluids, Relat. Interdiscip. Top.* **2016**, *93* (6), 063110.
(79) Shukla, V.; Volk, R.; Bourgoin, M.; Pumir, A. Phoresis in Turbulent Flows. *New J. Phys.* **2017**, *19* (12), 123030.
(80) Voth, G. A.; Soldati, A. Anisotropic Particles in Turbulence. *Annu. Rev. Fluid Mech.* **2017**, *49* (1), 249−276.
(81) Ounis, H.; Ahmadi, G. A Comparison of Brownian and Turbulent Diffusion. *Aerosol Sci. Technol.* **1990**, *13* (1), 47−53.
(82) Bourouiba, L.; Dehandschoewercker, E.; Bush, J. W. M. Violent Expiratory Events: on Coughing and Sneezing. *J. Fluid Mech.* **2014**, *745*, 537−563.
(83) Chen, C.; Lin, C.-H.; Jiang, Z.; Chen, Q. Simplified Models for Exhaled Airflow from a Cough with the Mouth Covered. *Indoor air* **2014**, *24* (6), 580−591.
(84) Noti, J. D.; Blachere, F. M.; McMillen, C. M.; Lindsley, W. G.; Kashon, M. L.; Slaughter, D. R.; Beezhold, D. H. High Humidity Leads to Loss of Infectious Influenza Virus from Simulated Coughs. *PLoS One* **2013**, *8* (2), No. e57485.
(85) Redrow, J.; Mao, S.; Celik, I.; Posada, J. A.; Feng, Z.-g. Modeling the Evaporation and Dispersion of Airborne Sputum Droplets Expelled from a Human Cough. *Building and Environment* **2011**, *46* (10), 2042−2051.
(86) Pendar, M.-R.; Páscoa, J. C. Numerical Modeling of the Distribution of Virus Carrying Saliva Droplets during Sneeze and Cough. *Phys. Fluids* **2020**, *32* (8), 083305.
(87) Ounis, H.; Ahmadi, G.; McLaughlin, J. B. Brownian Diffusion of Submicrometer Particles in the Viscous Sublayer. *J. Colloid Interface Sci.* **1991**, *143* (1), 266−277.
(88) Brooke, J. W.; Kontomaris, K.; Hanratty, T. J.; McLaughlin, J. B. Turbulent Deposition and Trapping of Aerosols at a Wall. *Phys. Fluids A* **1992**, *4* (4), 825−834.
(89) Goldman, A. J.; Cox, R. G.; Brenner, H. Slow Viscous Motion of a Sphere Parallel to a Plane Wall - I Motion through a Quiescent Fluid. *Chem. Eng. Sci.* **1967**, *22* (4), 637−651.
(90) Fan, F.-G.; Ahmadi, G. Wall Deposition of Small Ellipsoids from Turbulent Air Flows - A Brownian Dynamics Simulation. *J. Aerosol Sci.* **2000**, *31* (10), 1205−1229.
(91) Zhang, H.; Ahmadi, G. Aerosol Particle Transport and Deposition in Vertical and Horizontal Turbulent Duct Flows. *J. Fluid Mech.* **2000**, *406*, 55−80.
(92) He, C.; Ahmadi, G. Particle Deposition with Thermophoresis in Laminar and Turbulent Duct Flows. *Aerosol Sci. Technol.* **1998**, *29* (6), 525−546.
(93) Soldati, A.; Marchioli, C. Physics and Modelling of Turbulent Particle Deposition and Entrainment: Review of a Systematic Study. *Int. J. Multiphase Flow* **2009**, *35* (9), 827−839.
(94) Haber, S.; Butler, J. P.; Brenner, H.; Emanuel, I.; Tsuda, A. Shear Flow over a Self-Similar Expanding Pulmonary Alveolus during Rhythmical Breathing. *J. Fluid Mech.* **2000**, *405*, 243−268.
(95) Haber, S.; Yitzhak, D.; Tsuda, A. Gravitational Deposition in a Rhythmically Expanding and Contracting Alveolus. *J. Appl. Physiol.* **2003**, *95* (2), 657−671.
(96) Haber, S.; Yitzhak, D.; Tsuda, A. Trajectories and Deposition Sites of Spherical Particles Moving Inside Rhythmically Expanding Alveoli under Gravity-Free Conditions. *J. Aerosol Med. Pulm. Drug Delivery* **2010**, *23* (6), 405−413.
(97) Balásházy, I.; Hofmann, W.; Farkas, Á.; Madas, B. G. Three-Dimensional Model for Aerosol Transport and Deposition in Expanding and Contracting Alveoli. *Inhalation Toxicol.* **2008**, *20* (6), 611−621.
(98) Henry, F. S.; Laine-Pearson, F. E.; Tsuda, A. Hamiltonian Chaos in a Model Alveolus. *J. Biomech. Eng.* **2009**, *131* (1), 011006.
(99) Darquenne, C.; Paiva, M. Two- and Three-Dimensional Simulations of Aerosol Transport and Deposition in Alveolar Zone of Human Lung. *J. Appl. Physiol.* **1996**, *80* (4), 1401−1414.
(100) Ma, B.; Ruwet, V.; Corieri, P.; Theunissen, R.; Riethmuller, M.; Darquenne, C. CFD Simulation and Experimental Validation of Fluid Flow and Particle Transport in a Model of Alveolated Airways. *J. Aerosol Sci.* **2009**, *40* (5), 403−414.
(101) Darquenne, C. Aerosol Deposition in Health and Disease. *J. Aerosol Med. Pulm. Drug Delivery* **2012**, *25* (3), 140−147.
(102) Sznitman, J. Respiratory Microflows in the Pulmonary Acinus. *J. Biomech.* **2013**, *46* (2), 284−298.
(103) Longest, P. W.; Holbrook, L. T. In Silico Models of Aerosol Delivery to the Respiratory Tract - Development and Applications. *Adv. Drug Delivery Rev.* **2012**, *64* (4), 296−311.
(104) Pozrikidis, C. Interfacial Dynamics for Stokes Flow. *J. Comput. Phys.* **2001**, *169* (2), 250−301.
(105) Gubbiotti, A.; Chinappi, M.; Casciola, C. M. Confinement Effects on the Dynamics of a Rigid Particle in a Nanochannel. *Phys. Rev. E: Stat. Phys., Plasmas, Fluids, Relat. Interdiscip. Top.* **2019**, *100* (5), 053307.
(106) Ladd, A. J. C.; Verberg, R. Lattice-Boltzmann Simulations of Particle-Fluid Suspensions. *J. Stat. Phys.* **2001**, *104* (5), 1191−1251.
(107) Aidun, C. K.; Clausen, J. R. Lattice-Boltzmann Method for Complex Flows. *Annu. Rev. Fluid Mech.* **2010**, *42* (1), 439−472.
(108) Li, Z.; Kleinstreuer, C. Airflow Analysis in the Alveolar Region Using the Lattice-Boltzmann Method. *Med. Biol. Eng. Comput.* **2011**, *49* (4), 441−451.
(109) Teike, G.; Dietzel, M.; Michaelis, B.; Schomburg, H.; Sommerfeld, M. Multiscale Lattice−Boltzmann Approach for Electrophoretic Particle Deposition. *Aerosol Sci. Technol.* **2012**, *46* (4), 451−464.
(110) Wang, H.; Zhao, H.; Wang, K.; He, Y.; Zheng, C. Simulation of Filtration Process for Multi-Fiber Filter Using the Lattice-Boltzmann Two-Phase Flow Model. *J. Aerosol Sci.* **2013**, *66*, 164−178.
(111) Heyder, J. Deposition of Inhaled Particles in the Human Respiratory Tract and Consequences for Regional Targeting in Respiratory Drug Delivery. *Proc. Am. Thorac. Soc.* **2004**, *1* (4), 315−20.

https://dx.doi.org/10.1021/acsnano.0c08484
ACS Nano 2020, 14, 16502−16524

(112) Carvalho, T. C.; Peters, J. I.; Williams, R. O. Influence of Particle Size on Regional Lung Deposition − What Evidence is There? *Int. J. Pharm.* **2011**, *406* (1), 1−10.
(113) Hinds, W. C. *Aerosol Technology: Properties, Behavior, and Measurement of Airborne Particles*; Wiley: Hoboken, NJ, 1999.
(114) Garcia-Mouton, C.; Hidalgo, A.; Cruz, A.; Pérez-Gil, J. The Lord of the Lungs: The Essential Role of Pulmonary Surfactant upon Inhalation of Nanoparticles. *Eur. J. Pharm. Biopharm.* **2019**, *144*, 230−243.
(115) Ochs, M.; Nyengaard, J. R.; Jung, A.; Knudsen, L.; Voigt, M.; Wahlers, T.; Richter, J.; Gundersen, H. J. G. The Number of Alveoli in the Human Lung. *Am. J. Respir. Crit. Care Med.* **2004**, *169* (1), 120−124.
(116) Mutuku, J. K.; Hou, W. C.; Chen, W. H. An Overview of Experiments and Numerical Simulations on Airflow and Aerosols Deposition in Human Airways and the Role of Bioaerosol Motion in COVID-19 Transmission. *Aerosol Air Qual. Res.* **2020**, *20*, 1172−1196.
(117) Fernández Tena, A.; Casan Clarà, P. Deposition of Inhaled Particles in the Lungs. *Archivos de Bronconeumologia* **2012**, *48* (7), 240−246.
(118) Fahy, J. V.; Dickey, B. F. Airway Mucus Function and Dysfunction. *N. Engl. J. Med.* **2010**, *363* (23), 2233−47.
(119) Button, B.; Cai, L. H.; Ehre, C.; Kesimer, M.; Hill, D. B.; Sheehan, J. K.; Boucher, R. C.; Rubinstein, M. A Periciliary Brush Promotes the Lung Health by Separating the Mucus Layer from Airway Epithelia. *Science* **2012**, *337* (6097), 937−41.
(120) Stetten, A. Z.; Iasella, S. V.; Corcoran, T. E.; Garoff, S.; Przybycien, T. M.; Tilton, R. D. Surfactant-Induced Marangoni Transport of Lipids and Therapeutics within the Lung. *Curr. Opin. Colloid Interface Sci.* **2018**, *36*, 58−69.
(121) Geiser, M.; Kreyling, W. G. Deposition and Biokinetics of Inhaled Nanoparticles. *Part. Fibre Toxicol.* **2010**, *7* (1), 2.
(122) Ruge, C. A.; Kirch, J.; Lehr, C. M. Pulmonary Drug Delivery: From Generating Aerosols to Overcoming Biological Barriers - Therapeutic Possibilities and Technological Challenges. *Lancet Respir. Med.* **2013**, *1* (5), 402−13.
(123) Ruge, C. A.; Schaefer, U. F.; Herrmann, J.; Kirch, J.; Cañadas, O.; Echaide, M.; Pérez-Gil, J.; Casals, C.; Müller, R.; Lehr, C. M. The Interplay of Lung Surfactant Proteins and Lipids Assimilates the Macrophage Clearance of Nanoparticles. *PLoS One* **2012**, *7* (7), No. e40775.
(124) Ruge, C. A.; Kirch, J.; Cañadas, O.; Schneider, M.; Perez-Gil, J.; Schaefer, U. F.; Casals, C.; Lehr, C. M. Uptake of Nanoparticles by Alveolar Macrophages is Triggered by Surfactant Protein A. *Nanomedicine* **2011**, *7* (6), 690−3.
(125) Geiser, M. Update on Macrophage Clearance of Inhaled Micro- and Nanoparticles. *J. Aerosol Med. Pulm. Drug Delivery* **2010**, *23* (4), 207−17.
(126) Sungnak, W.; Huang, N.; Bécavin, C.; Berg, M.; Queen, R.; Litvinukova, M.; Talavera-López, C.; Maatz, H.; Reichart, D.; Sampaziotis, F.; Worlock, K. B.; Yoshida, M.; Barnes, J. L.; Banovich, N. E.; Barbry, P.; Brazma, A.; Collin, J.; Desai, T. J.; Duong, T. E.; Eickelberg, O.; et al. SARS-CoV-2 Entry Factors are Highly Expressed in Nasal Epithelial Cells Together with Innate Immune Genes. *Nat. Med.* **2020**, *26* (5), 681−687.
(127) Wilson, N. M.; Norton, A.; Young, F. P.; Collins, D. W. Airborne Transmission of Severe Acute Respiratory Syndrome Coronavirus-2 to Healthcare Workers: A Narrative Review. *Anaesthesia* **2020**, *75* (8), 1086−1095.
(128) Mason, R. J. Thoughts on the Alveolar Phase of COVID-19. *Am. J. Physiol Lung Cell Mol. Physiol* **2020**, *319* (1), L115−L120.
(129) Mason, R. J. Pathogenesis of COVID-19 from a Cell Biology Perspective. *Eur. Respir. J.* **2020**, *55* (4), 2000607.
(130) Zhou, F.; Yu, T.; Du, R.; Fan, G.; Liu, Y.; Liu, Z.; Xiang, J.; Wang, Y.; Song, B.; Gu, X.; Guan, L.; Wei, Y.; Li, H.; Wu, X.; Xu, J.; Tu, S.; Zhang, Y.; Chen, H.; Cao, B. Clinical Course and Risk Factors for Mortality of Adult Inpatients with COVID-19 in Wuhan, China: A Retrospective Cohort Study. *Lancet* **2020**, *395* (10229), 1054−1062.
(131) Machhi, J.; Herskovitz, J.; Senan, A. M.; Dutta, D.; Nath, B.; Oleynikov, M. D.; Blomberg, W. R.; Meigs, D. D.; Hasan, M.; Patel, M.; Kline, P.; Chang, R. C.; Chang, L.; Gendelman, H. E.; Kevadiya, B. D. The Natural History, Pathobiology, and Clinical Manifestations of SARS-CoV-2 Infections. *Journal of Neuroimmune Pharmacology* **2020**, *15* (3), 359−386.
(132) Fan, E.; Beitler, J. R.; Brochard, L.; Calfee, C. S.; Ferguson, N. D.; Slutsky, A. S.; Brodie, D. COVID-19-Associated Acute Respiratory Distress Syndrome: Is a Different Approach to Management Warranted? *Lancet Respir. Med.* **2020**, *8* (8), 816−821.
(133) Hoffmann, M.; Kleine-Weber, H.; Schroeder, S.; Krüger, N.; Herrler, T.; Erichsen, S.; Schiergens, T. S.; Herrler, G.; Wu, N.-H.; Nitsche, A.; Müller, M. A.; Drosten, C.; Pöhlmann, S. SARS-CoV-2 Cell Entry Depends on ACE2 and TMPRSS2 and Is Blocked by a Clinically Proven Protease Inhibitor. *Cell* **2020**, *181* (2), 271−280.
(134) Hou, Y. J.; Okuda, K.; Edwards, C. E.; Martinez, D. R.; Asakura, T.; Dinnon, K. H.; Kato, T.; Lee, R. E.; Yount, B. L.; Mascenik, T. M.; Chen, G.; Olivier, K. N.; Ghio, A.; Tse, L. V.; Leist, S. R.; Gralinski, L. E.; Schäfer, A.; Dang, H.; Gilmore, R.; Nakano, S.; et al. SARS-CoV-2 Reverse Genetics Reveals a Variable Infection Gradient in the Respiratory Tract. *Cell* **2020**, *182* (2), 429−446.
(135) Zuo, Y. Y.; Veldhuizen, R. A.; Neumann, A. W.; Petersen, N. O.; Possmayer, F. Current Perspectives in Pulmonary Surfactant - Inhibition, Enhancement and Evaluation. *Biochim. Biophys. Acta, Biomembr.* **2008**, *1778* (10), 1947−77.
(136) Zhang, H.; Fan, Q.; Wang, Y. E.; Neal, C. R.; Zuo, Y. Y. Comparative Study of Clinical Pulmonary Surfactants using Atomic Force Microscopy. *Biochim. Biophys. Acta, Biomembr.* **2011**, *1808* (7), 1832−42.
(137) Zhang, H.; Wang, Y. E.; Fan, Q.; Zuo, Y. Y. On the Low Surface Tension of Lung Surfactant. *Langmuir* **2011**, *27* (13), 8351−8.
(138) Autilio, C.; Perez-Gil, J. Understanding the Principle Biophysics Concepts of Pulmonary Surfactant in Health and Disease. *Arch. Dis. Child. Fetal Neonatal Ed.* **2018**, *104* (4), F443−F451.
(139) Guagliardo, R.; Perez-Gil, J.; De Smedt, S.; Raemdonck, K. Pulmonary Surfactant and Drug Delivery: Focusing on the Role of Surfactant Proteins. *J. Controlled Release* **2018**, *291*, 116−126.
(140) Cañadas, O.; Olmeda, B.; Alonso, A.; Pérez-Gil, J. Lipid-Protein and Protein-Protein Interactions in the Pulmonary Surfactant System and Their Role in Lung Homeostasis. *Int. J. Mol. Sci.* **2020**, *21* (10), 3708.
(141) Tsuda, A.; Gehr, P. *Nanoparticles in the Lung: Environmental Exposure and Drug Delivery*; CRC Press: Boca Raton, FL, 2015.
(142) Hidalgo, A.; Cruz, A.; Pérez-Gil, J. Pulmonary Surfactant and Nanocarriers: Toxicity *versus* Combined Nanomedical Applications. *Biochim. Biophys. Acta, Biomembr.* **2017**, *1859* (9), 1740−1748.
(143) Leth-Larsen, R.; Zhong, F.; Chow, V. T.; Holmskov, U.; Lu, J. The SARS coronavirus Spike Glycoprotein Is Selectively Recognized by Lung Surfactant Protein D and Activates Macrophages. *Immunobiology* **2007**, *212* (3), 201−11.
(144) Fan, Q.; Wang, Y. E.; Zhao, X.; Loo, J. S.; Zuo, Y. Y. Adverse Biophysical Effects of Hydroxyapatite Nanoparticles on Natural Pulmonary Surfactant. *ACS Nano* **2011**, *5* (8), 6410−6.
(145) Hu, G.; Jiao, B.; Shi, X.; Valle, R. P.; Fan, Q.; Zuo, Y. Y. Physicochemical Properties of Nanoparticles Regulate Translocation across Pulmonary Surfactant Monolayer and Formation of Lipoprotein Corona. *ACS Nano* **2013**, *7* (12), 10525−33.
(146) Valle, R. P.; Wu, T.; Zuo, Y. Y. Biophysical Influence of Airborne Carbon Nanomaterials on Natural Pulmonary Surfactant. *ACS Nano* **2015**, *9* (5), 5413−21.
(147) Valle, R. P.; Huang, C. L.; Loo, J. S. C.; Zuo, Y. Y. Increasing Hydrophobicity of Nanoparticles Intensifies Lung Surfactant Film Inhibition and Particle Retention. *ACS Sustainable Chem. Eng.* **2014**, *2* (7), 1574−1580.
(148) Yang, Y.; Xu, L.; Dekkers, S.; Zhang, L. G.; Cassee, F. R.; Zuo, Y. Y. Aggregation State of Metal-Based Nanomaterials at the Pulmonary Surfactant Film Determines Biophysical Inhibition. *Environ. Sci. Technol.* **2018**, *52* (15), 8920−8929.

https://dx.doi.org/10.1021/acsnano.0c08484
ACS Nano 2020, 14, 16502−16524

(149) Sorli, J. B.; Huang, Y.; Da Silva, E.; Hansen, J. S.; Zuo, Y. Y.; Frederiksen, M.; Norgaard, A. W.; Ebbehoj, N. E.; Larsen, S. T.; Hougaard, K. S. Prediction of Acute Inhalation Toxicity using *in Vitro* Lung Surfactant Inhibition. *Altex* **2018**, *35* (1), 26−36.
(150) Sorli, J. B.; Balogh Sivars, K.; Da Silva, E.; Hougaard, K. S.; Koponen, I. K.; Zuo, Y. Y.; Weydahl, I. E. K.; Aberg, P. M.; Fransson, R. Bile Salt Enhancers for Inhalation: Correlation between *in Vitro* and *in Vivo* Lung Effects. *Int. J. Pharm.* **2018**, *550* (1−2), 114−122.
(151) Chen, Y.; Yang, Y.; Xu, B.; Wang, S.; Li, B.; Ma, J.; Gao, J.; Zuo, Y. Y.; Liu, S. Mesoporous Carbon Nanomaterials Induced Pulmonary Surfactant Inhibition, Cytotoxicity, Inflammation and Lung Fibrosis. *J. Environ. Sci.* **2017**, *62*, 100−114.
(152) Wu, Y.; Guo, Y.; Song, H.; Liu, W.; Yang, Y.; Liu, Y.; Sang, N.; Zuo, Y. Y.; Liu, S. Oxygen Content Determines the Bio-Reactivity and Toxicity Profiles of Carbon Black Particles. *Ecotoxicol. Environ. Saf.* **2018**, *150*, 207−214.
(153) Yang, Y.; Wu, Y.; Ren, Q.; Zhang, L. G.; Liu, S.; Zuo, Y. Y. Biophysical Assessment of Pulmonary Surfactant Predicts the Lung Toxicity of Nanomaterials. *Small Methods* **2018**, *2* (4), 1700367.
(154) Numata, M.; Mitchell, J. R.; Tipper, J. L.; Brand, J. D.; Trombley, J. E.; Nagashima, Y.; Kandasamy, P.; Chu, H. W.; Harrod, K. S.; Voelker, D. R. Pulmonary Surfactant Lipids Inhibit Infections with the Pandemic H1N1 Influenza Virus in Several Animal Models. *J. Biol. Chem.* **2020**, *295* (6), 1704−1715.
(155) Veldhuizen, R. A.; Yao, L.-J.; Hearn, S. A.; Possmayer, F.; Lewis, J. F. Surfactant-Associated Protein A Is Important for Maintaining Surfactant Large-Aggregate Forms during Surface-Area Cycling. *Biochem. J.* **1996**, *313* (3), 835−840.
(156) Veldhuizen, R. A.; Ito, Y.; Marcou, J.; Yao, L. J.; McCaig, L.; Lewis, J. F. Effects of Lung Injury on Pulmonary Surfactant Aggregate Conversion *in Vivo* and *in Vitro*. *Am. J. Physiol.* **1997**, *272* (5), L872−L878.
(157) Quintero, O. A.; Wright, J. R. Clearance of Surfactant Lipids by Neutrophils and Macrophages Isolated From the Acutely Inflamed Lung. *Am. J. Physiol Lung Cell Mol. Physiol* **2002**, *282* (2), L330−9.
(158) Busani, S.; Dall'Ara, L.; Tonelli, R.; Clini, E.; Munari, E.; Venturelli, S.; Meschiari, M.; Guaraldi, G.; Cossarizza, A.; Ranieri, V. M.; Girardis, M. Surfactant Replacement Might Help Recovery of Low-Compliance Lung in Severe COVID-19 Pneumonia. *Ther. Adv. Respir. Dis.* **2020**, *14*, 175346662095104.
(159) Hu, Q.; Bai, X.; Hu, G.; Zuo, Y. Y. Unveiling the Molecular Structure of Pulmonary Surfactant Corona on Nanoparticles. *ACS Nano* **2017**, *11* (7), 6832−6842.
(160) Cedervall, T.; Lynch, I.; Lindman, S.; Berggard, T.; Thulin, E.; Nilsson, H.; Dawson, K. A.; Linse, S. Understanding the Nanoparticle-Protein Corona Using Methods to Quantify Exchange Rates and Affinities of Proteins for Nanoparticles. *Proc. Natl. Acad. Sci. U. S. A.* **2007**, *104* (7), 2050−5.
(161) Lynch, I.; Dawson, K. A. Protein-Nanoparticle Interactions. *Nano Today* **2008**, *3* (1−2), 40−47.
(162) Monopoli, M. P.; Aberg, C.; Salvati, A.; Dawson, K. A. Biomolecular Coronas Provide the Biological Identity of Nanosized Materials. *Nat. Nanotechnol.* **2012**, *7* (12), 779−86.
(163) Ke, P. C.; Lin, S.; Parak, W. J.; Davis, T. P.; Caruso, F. A Decade of the Protein Corona. *ACS Nano* **2017**, *11* (12), 11773−11776.
(164) Nel, A. E.; Madler, L.; Velegol, D.; Xia, T.; Hoek, E. M.; Somasundaran, P.; Klaessig, F.; Castranova, V.; Thompson, M. Understanding Biophysicochemical Interactions at the Nano-Bio Interface. *Nat. Mater.* **2009**, *8* (7), 543−57.
(165) Aggarwal, P.; Hall, J. B.; McLeland, C. B.; Dobrovolskaia, M. A.; McNeil, S. E. Nanoparticle Interaction with Plasma Proteins as It Relates to Particle Biodistribution, Biocompatibility and Therapeutic Efficacy. *Adv. Drug Delivery Rev.* **2009**, *61* (6), 428−37.
(166) Raesch, S. S.; Tenzer, S.; Storck, W.; Rurainski, A.; Selzer, D.; Ruge, C. A.; Perez-Gil, J.; Schaefer, U. F.; Lehr, C. M. Proteomic and Lipidomic Analysis of Nanoparticle Corona upon Contact with Lung Surfactant Reveals Differences in Protein, but Not Lipid Composition. *ACS Nano* **2015**, *9* (12), 11872−85.
(167) Kapralov, A. A.; Feng, W. H.; Amoscato, A. A.; Yanamala, N.; Balasubramanian, K.; Winnica, D. E.; Kisin, E. R.; Kotchey, G. P.; Gou, P.; Sparvero, L. J.; Ray, P.; Mallampalli, R. K.; Klein-Seetharaman, J.; Fadeel, B.; Star, A.; Shvedova, A. A.; Kagan, V. E. Adsorption of Surfactant Lipids by Single-Walled Carbon Nanotubes in Mouse Lung Upon Pharyngeal Aspiration. *ACS Nano* **2012**, *6* (5), 4147−56.
(168) Thorley, A. J.; Ruenraroengsak, P.; Potter, T. E.; Tetley, T. D. Critical Determinants of Uptake and Translocation of Nanoparticles by the Human Pulmonary Alveolar Epithelium. *ACS Nano* **2014**, *8* (11), 11778−11789.
(169) Vranic, S.; Garcia-Verdugo, I.; Darnis, C.; Sallenave, J. M.; Boggetto, N.; Marano, F.; Boland, S.; Baeza-Squiban, A. Internalization of SiO2 Nanoparticles by Alveolar Macrophages and Lung Epithelial Cells and Its Modulation by the Lung Surfactant Substitute Curosurf. *Environ. Sci. Pollut. Res.* **2013**, *20* (5), 2761−70.
(170) Cao, Z.; Tsai, S. N.; Zuo, Y. Y. An Optical Method for Quantitatively Determining the Surface Free Energy of Micro- and Nanoparticles. *Anal. Chem.* **2019**, *91* (20), 12819−12826.
(171) Sund, J.; Alenius, H.; Vippola, M.; Savolainen, K.; Puustinen, A. Proteomic Characterization of Engineered Nanomaterial-Protein Interactions in Relation to Surface Reactivity. *ACS Nano* **2011**, *5* (6), 4300−9.
(172) Schulze, C.; Schaefer, U. F.; Ruge, C. A.; Wohlleben, W.; Lehr, C. M. Interaction of Metal Oxide Nanoparticles with Lung Surfactant Protein A. *Eur. J. Pharm. Biopharm.* **2011**, *77* (3), 376−83.
(173) Schleh, C.; Holzwarth, U.; Hirn, S.; Wenk, A.; Simonelli, F.; Schaffler, M.; Moller, W.; Gibson, N.; Kreyling, W. G. Biodistribution of Inhaled Gold Nanoparticles in Mice and the Influence of Surfactant Protein D. *J. Aerosol Med. Pulm. Drug Delivery* **2013**, *26* (1), 24−30.
(174) Evans, M. Avoiding COVID-19: Aerosol Guidelines. *medRxiv*, June 5, 2020, ver. 1.https://www.medrxiv.org/content/10.1101/2020.05.21.20108894v3 (accessed 2020-06-05).
(175) Buonanno, G.; Morawska, L.; Stabile, L. Quantitative Assessment of the Risk of Airborne Transmission of SARS-CoV-2 Infection: Prospective and Retrospective applications. *Environ. Int.* **2020**, *145*, 106112.
(176) Wrapp, D.; Wang, N.; Corbett, K. S.; Goldsmith, J. A.; Hsieh, C.-L.; Abiona, O.; Graham, B. S.; McLellan, J. S. Cryo-EM Structure of the 2019-nCoV Spike in the Prefusion Conformation. *Science* **2020**, *367* (6483), 1260−1263.
(177) Walls, A. C.; Tortorici, M. A.; Bosch, B.-J.; Frenz, B.; Rottier, P. J.; DiMaio, F.; Rey, F. A.; Veesler, D. Cryo-Electron Microscopy Structure of a Coronavirus Spike Glycoprotein Trimer. *Nature* **2016**, *531* (7592), 114−117.
(178) Walls, A. C.; Park, Y.-J.; Tortorici, M. A.; Wall, A.; McGuire, A. T.; Veesler, D. Structure, Function, and Antigenicity of the SARS-CoV-2 Spike Glycoprotein. *Cell* **2020**, *181* (2), 281−292.
(179) Yan, R.; Zhang, Y.; Li, Y.; Xia, L.; Guo, Y.; Zhou, Q. Structural Basis for the Recognition of SARS-CoV-2 by Full-Length Human ACE2. *Science* **2020**, *367* (6485), 1444−1448.
(180) Woo, H.; Park, S.-J.; Choi, Y. K.; Park, T.; Tanveer, M.; Cao, Y.; Kern, N. R.; Lee, J.; Yeom, M. S.; Croll, T. I.; Seok, C.; Im, W. Developing a Fully-Glycosylated Full-Length SARS-CoV-2 Spike Protein Model in a Viral Membrane. *J. Phys. Chem. B* **2020**, *124* (33), 7128−7137.
(181) Casalino, L.; Gaieb, Z.; Goldsmith, J. A.; Hjorth, C. K.; Dommer, A. C.; Harbison, A. M.; Fogarty, C. A.; Barros, E. P.; Taylor, B. C.; McLellan, J. S.; Fadda, E.; Amaro, R. E. Beyond Shielding: The Roles of Glycans in SARS-CoV-2 Spike Protein. *ACS Cent. Sci.* **2020**, *6* (10), 1722−1734.
(182) Turoňová, B.; Sikora, M.; Schürmann, C.; Hagen, W. J.; Welsch, S.; Blanc, F. E.; von Bülow, S.; Gecht, M.; Bagola, K.; Hörner, C.; et al. *In Situ* Structural Analysis of SARS-CoV-2 Spike Reveals Flexibility Mediated by Three Hinges. *Science* **2020**, *370* (6513), 203−208.
(183) Ali, A.; Vijayan, R. Dynamics of the ACE2−SARS-CoV-2/SARS-CoV Spike Protein Interface Reveal Unique Mechanisms. *Sci. Rep.* **2020**, *10* (1), 14214.
(184) Serapian, S. A.; Marchetti, F.; Triveri, A.; Morra, G.; Meli, M.; Moroni, E.; Sautto, G. A.; Rasola, A.; Colombo, G. The Answer Lies in

https://dx.doi.org/10.1021/acsnano.0c08484
ACS Nano 2020, 14, 16502−16524

the Energy: How Simple Atomistic Molecular Dynamics Simulations May Hold the Key to Epitope Prediction on the Fully Glycosylated SARS-CoV-2 Spike Protein. *J. Phys. Chem. Lett.* **2020**, *11* (19), 8084−8093.
(185) Frenkel, D.; Smit, B. *Understanding Molecular Simulation: From Algorithms to Applications*, 2nd ed; Academic Press: San Diego, 2001.
(186) Warshel, A. *Computer Modeling of Chemical Reactions in Enzymes and Solutions*; Wiley: New York, 1991.
(187) Durrant, J. D.; Kochanek, S. E.; Casalino, L.; Ieong, P. U.; Dommer, A. C.; Amaro, R. E. Mesoscale All-Atom Influenza Virus Simulations Suggest New Substrate Binding Mechanism. *ACS Cent. Sci.* **2020**, *6* (2), 189−196.
(188) Shekhar, A.; Nomura, K.-i.; Kalia, R. K.; Nakano, A.; Vashishta, P. Nanobubble Collapse on a Silica Surface in Water: Billion-Atom Reactive Molecular Dynamics Simulations. *Phys. Rev. Lett.* **2013**, *111* (18), 184503.
(189) Shaw, D. E.; Maragakis, P.; Lindorff-Larsen, K.; Piana, S.; Dror, R. O.; Eastwood, M. P.; Bank, J. A.; Jumper, J. M.; Salmon, J. K.; Shan, Y.; Wriggers, W. Atomic-Level Characterization of the Structural Dynamics of Proteins. *Science* **2010**, *330* (6002), 341−346.
(190) Wei, T.; Carignano, M. A.; Szleifer, I. Molecular Dynamics Simulation of Lysozyme Adsorption/Desorption on Hydrophobic Surfaces. *J. Phys. Chem. B* **2012**, *116* (34), 10189−10194.
(191) Wei, T.; Huang, T.; Qiao, B.; Zhang, M.; Ma, H.; Zhang, L. Structures, Dynamics, and Water Permeation Free Energy across Bilayers of Lipid A and Its Analog Studied with Molecular Dynamics Simulation. *J. Phys. Chem. B* **2014**, *118* (46), 13202−13209.
(192) Wei, T.; Sajib, M. S. J.; Samieegohar, M.; Ma, H.; Shing, K. Self-Assembled Monolayers of an Azobenzene Derivative on Silica and Their Interactions with Lysozyme. *Langmuir* **2015**, *31* (50), 13543−13552.
(193) Zheng, J.; Li, L.; Tsao, H.-K.; Sheng, Y.-J.; Chen, S.; Jiang, S. Strong Repulsive Forces between Protein and Oligo (Ethylene Glycol) Self-Assembled Monolayers: A Molecular Simulation Study. *Biophys. J.* **2005**, *89* (1), 158−166.
(194) Nakano, C. M.; Ma, H.; Wei, T. Study of Lysozyme Mobility and Binding Free Energy during Adsorption on a Graphene Surface. *Appl. Phys. Lett.* **2015**, *106* (15), 153701.
(195) Wei, T.; Carignano, M. A.; Szleifer, I. Lysozyme Adsorption on Polyethylene Surfaces: Why Are Long Simulations Needed? *Langmuir* **2011**, *27* (19), 12074−12081.
(196) Amaro, R. E.; Mulholland, A. J. A Community Letter Regarding Sharing Biomolecular Simulation Data for COVID-19. *J. Chem. Inf. Model.* **2020**, *60* (6), 2653−2656.
(197) Watanabe, Y.; Allen, J. D.; Wrapp, D.; McLellan, J. S.; Crispin, M. Site-Specific Glycan Analysis of the SARS-CoV-2 Spike. *Science* **2020**, *369* (6501), 330−333.
(198) Shajahan, A.; Supekar, N. T.; Gleinich, A. S.; Azadi, P. Deducing the N-and O-Glycosylation Profile of the Spike Protein of Novel Coronavirus SARS-CoV-2. *Glycobiology* **2020**, cwaa042.
(199) Brooks, B. R.; Bruccoleri, R. E.; Olafson, B. D.; States, D. J.; Swaminathan, S. A.; Karplus, M. CHARMM: A Program for Macromolecular Energy, Minimization, and Dynamics Calculations. *J. Comput. Chem.* **1983**, *4* (2), 187−217.
(200) MacKerell, A. D., Jr; Bashford, D.; Bellott, M.; Dunbrack, R. L., Jr; Evanseck, J. D.; Field, M. J.; Fischer, S.; Gao, J.; Guo, H.; Ha, S.; et al. All-Atom Empirical Potential for Molecular Modeling and Dynamics Studies of Proteins. *J. Phys. Chem. B* **1998**, *102* (18), 3586−3616.
(201) Mallajosyula, S. S.; Guvench, O.; Hatcher, E.; MacKerell, A. D., Jr CHARMM Additive All-Atom Force Field for Phosphate and Sulfate Linked to Carbohydrates. *J. Chem. Theory Comput.* **2012**, *8* (2), 759−776.
(202) Cornell, W. D.; Cieplak, P.; Bayly, C. I.; Gould, I. R.; Merz, K. M.; Ferguson, D. M.; Spellmeyer, D. C.; Fox, T.; Caldwell, J. W.; Kollman, P. A. A Second Generation Force Field for the Simulation of Proteins, Nucleic Acids, and Organic Molecules. *J. Am. Chem. Soc.* **1995**, *117* (19), 5179−5197.
(203) Duan, Y.; Wu, C.; Chowdhury, S.; Lee, M. C.; Xiong, G.; Zhang, W.; Yang, R.; Cieplak, P.; Luo, R.; Lee, T.; et al. A Point-Charge Force Field for Molecular Mechanics Simulations of Proteins Based on Condensed-Phase Quantum Mechanical Calculations. *J. Comput. Chem.* **2003**, *24* (16), 1999−2012.
(204) Maier, J. A.; Martinez, C.; Kasavajhala, K.; Wickstrom, L.; Hauser, K. E.; Simmerling, C. ff14SB: Improving the Accuracy of Protein Side Chain and Backbone Parameters from ff99SB. *J. Chem. Theory Comput.* **2015**, *11* (8), 3696−3713.
(205) Jorgensen, W. L.; Maxwell, D. S.; Tirado-Rives, J. Development and Testing of the OPLS All-Atom Force Field on Conformational Energetics and Properties of Organic Liquids. *J. Am. Chem. Soc.* **1996**, *118* (45), 11225−11236.
(206) Kony, D.; Damm, W.; Stoll, S.; Van Gunsteren, W. F. An Improved OPLS-AA Force Field for Carbohydrates. *J. Comput. Chem.* **2002**, *23* (15), 1416−1429.
(207) Voth, G. A. *Coarse-Graining of Condensed Phase and Biomolecular Systems*; CRC Press: Boca Raton, 2008.
(208) Kmiecik, S.; Gront, D.; Kolinski, M.; Wieteska, L.; Dawid, A. E.; Kolinski, A. Coarse-Grained Protein Models and Their Applications. *Chem. Rev.* **2016**, *116* (14), 7898−7936.
(209) Marrink, S. J.; Risselada, H. J.; Yefimov, S.; Tieleman, D. P.; De Vries, A. H. The MARTINI Force Field: Coarse Grained Model for Biomolecular Simulations. *J. Phys. Chem. B* **2007**, *111* (27), 7812−7824.
(210) Woo, H.; Park, S.-J.; Choi, Y. K.; Park, T.; Tanveer, M.; Cao, Y.; Kern, N. R.; Lee, J.; Yeom, M. S.; Croll, T.; Seok, C.; Im, W. Developing a Fully Glycosylated Full-Length SARS-CoV-2 Spike Protein Model in a Viral Membrane. *J. Phys. Chem. B* **2020**, *124* (33), 7128−7137.
(211) Webb, M. A.; Delannoy, J.-Y.; De Pablo, J. J. Graph-Based Approach to Systematic Molecular Coarse-Graining. *J. Chem. Theory Comput.* **2019**, *15* (2), 1199−1208.
(212) Parks, J. M.; Smith, J. C. How to Discover Antiviral Drugs Quickly. *N. Engl. J. Med.* **2020**, *382* (23), 2261−2264.
(213) Baig, M. S.; Alagumuthu, M.; Rajpoot, S.; Saqib, U. Identification of a Potential Peptide Inhibitor of SARS-CoV-2 Targeting Its Entry into the Host Cells. *Drugs R&D* **2020**, *20* (3), 161−169.
(214) Zhang, C.; Zheng, W.; Huang, X.; Bell, E. W.; Zhou, X.; Zhang, Y. Protein Structure and Sequence Re-Analysis of 2019-nCoV Genome Does Not Indicate Snakes as its Intermediate Host or the Unique Similarity between its Spike Protein Insertions and HIV-1. *J. Proteome Res.* **2020**, *19*, 1351−1360.
(215) Buehler, M. J. Nanomechanical Sonification of the 2019-nCoV Coronavirus Spike Protein through a Materiomusical Approach. *arXiv (Popular Physics)*, March 30, 2020, 2003.14258, ver.1. https://arxiv.org/abs/2003.14258 (accessed 2020-03-30).
(216) Gur, M.; Taka, E.; Yilmaz, S. Z.; Kilinc, C.; Aktas, U.; Golcuk, M. Exploring Conformational Transition of 2019 Novel Coronavirus Spike Glycoprotein Between Its Closed and Open States Using Molecular Dynamics Simulations. *J. Chem. Phys.* **2020**, *153*, 075101.
(217) Letko, M.; Marzi, A.; Munster, V. Functional Assessment of Cell Entry and Receptor Usage for SARS-CoV-2 and Other Lineage B Betacoronaviruses. *Nature Microbiology* **2020**, *5* (4), 562−569.
(218) Lan, J.; Ge, J.; Yu, J.; Shan, S.; Zhou, H.; Fan, S.; Zhang, Q.; Shi, X.; Wang, Q.; Zhang, L.; Wang, X. Structure of the SARS-CoV-2 Spike Receptor-Binding Domain Bound to the ACE2 Receptor. *Nature* **2020**, *581* (7807), 215−220.
(219) Hati, S.; Bhattacharyya, S. Impact of Thiol-Disulfide Balance on the Binding of Covid-19 Spike Protein with Angiotensin Converting Enzyme 2 Receptor. *ACS Omega* **2020**, *5* (26), 16292−16298.
(220) Wang, J.; Xu, X.; Zhou, X.; Chen, P.; Liang, H.; Li, X.; Zhong, W.; Hao, P. Molecular Simulation of SARS-CoV-2 Spike Protein Binding to Pangolin ACE2 or Human ACE2 Natural Variants Reveals Altered Susceptibility to Infection. *J. Gen. Virol.* **2020**, *101* (9), 921−924.
(221) Han, Y.; Král, P. Computational Design of ACE2-Based Peptide Inhibitors of SARS-CoV-2. *ACS Nano* **2020**, *14* (4), 5143−5147.
(222) Qiao, B.; Olvera de la Cruz, M. Enhanced Binding of SARS-CoV-2 Spike Protein to Receptor by Distal Polybasic Cleavage Sites. *ACS Nano* **2020**, *14* (8), 10616−10623.

https://dx.doi.org/10.1021/acsnano.0c08484
ACS Nano 2020, 14, 16502−16524